

Universal radiation tolerant semiconductor

Alexander Azarov^{1*}, Javier García Fernández¹, Junlei Zhao², Flyura Djurabekova³,
Huan He³, Ru He³, Øystein Prytz¹, Lasse Vines¹, Umutcan Bektas⁴, Paul Chekhonin⁴,
Nico Klingner⁴, Gregor Hlawacek⁴ and Andrej Kuznetsov^{1*}

¹ *University of Oslo, Centre for Materials Science and Nanotechnology, PO Box 1048 Blindern,
N-0316 Oslo, Norway*

² *Department of Electrical and Electronic Engineering, Southern University of Science and
Technology, Shenzhen 518055, China*

³ *Department of Physics, University of Helsinki, P.O. Box 43, FI-00014 Helsinki, Finland*

⁴ *Helmholtz-Zentrum Dresden-Rossendorf, D-01328 Dresden, Germany*

* Authors to whom correspondence should be addressed:

andrej.kuznetsov@fys.uio.no (AK)

alexander.azarov@smn.uio.no (AA)

Summary

Radiation tolerance is determined as an ability of crystalline materials to withstand the accumulation of the radiation induced disorder. Based on the magnitudes of such disorder levels, semiconductors are commonly grouped into the low- or high-radiation tolerant. Nevertheless, upon exposing to sufficiently high fluences, in all cases known by far, it ends up with either extremely high disorder levels or amorphization. Here we show that gamma/beta double polymorph Ga_2O_3 structures exhibit unprecedentedly high radiation tolerance. Specifically, for room temperature experiments, they tolerate a disorder equivalent to hundreds of displacements per atom, without severe degradations of crystallinity; in comparison with, e.g., Si amorphizable already with the lattice atoms displaced just once. We explain this behavior by an interesting combination of the Ga- and O-sublattice properties in gamma- Ga_2O_3 . In particular, O-sublattice exhibits a strong recrystallization trend to recover the face-centered-cubic stacking despite high mobility of O atoms in collision cascades compared to Ga. Concurrently, the characteristic structure of the Ga-sublattice is nearly insensitive to the accumulated disorder. Jointly it explains macroscopically negligible structural deformations in gamma- Ga_2O_3 observed in experiment. Notably, we also explained the origin of the beta-to-gamma Ga_2O_3 transformation, as a function of increased disorder in beta- Ga_2O_3 and studied the phenomena as a function of the chemical nature of the implanted atoms. As a result, we conclude that gamma-beta double polymorph Ga_2O_3 structures, in terms of their radiation tolerance properties, benchmark a new class of universal radiation tolerant semiconductors.

Long-range periodicity or translation symmetry is a unique property of solids, even though solids may form amorphous phases too. In this context, accelerated particle beam irradiations are known to induce amorphization in many types of crystals, e.g. in semiconductors [1,2]. In its turn, radiation tolerance in semiconductors is determined as an ability to withstand the accumulation of the radiation disorder, otherwise leading to highly disordered lattice and, upon irradiating with sufficiently high fluences, to amorphization [3,4]. The irradiation-induced disordering mechanisms are generic, even though exhibiting material-specific differences, allowing to classify semiconductors as low- or high-radiation tolerant [5-8]. Importantly, very recently, it was discovered that in gallium oxide (Ga_2O_3), which is a promising material for the next generation power electronics [9-11], the amorphization may be prominently suppressed by the formation of a new metastable crystalline polymorph phase [14]. This process occurs in the irradiation interaction volume and results in a new polymorph film, separated from the initial polymorph by a sharp interface. In this paper, we report that such double polymorph Ga_2O_3 structures exhibit unprecedentedly high radiation tolerance. Specifically, for room temperature experiments, these samples tolerated a disorder equivalent to hundreds of displacements per atom (DPA), without severe degradations of the crystallinity. For comparison, other semiconductors studied in literature for comparative DPAs, either amorphized or exhibit high degree of the lattice disorder. Notably, to induce such high DPAs we used high fluence ion irradiations creating high excess of implanted atoms, maximized at the depth of the ion range, and affecting the process depending on the chemical nature of the implanted atoms.

Fig. 1 illustrates such high radiation tolerance of the double polymorph Ga_2O_3 structures, tolerating up to 265 DPA (see Supplementary Materials (SM) I for the DPA calculations) without severe degradation in crystallinity (panels (a)–(c)), set in a context of the same characteristics in other semiconductors (panel (d)). Fig. 1(a) plots the

RBS/C spectra of the double polymorph Ga_2O_3 structure as a function of the fluence in the range of $1 \times 10^{16} - 1 \times 10^{17} \text{ Ni/cm}^2$. As explained in Methods and in more details in SM-II, the characteristic shape observed for the $1 \times 10^{16} \text{ Ni/cm}^2$ RBS/C spectrum is a fingerprint of the high crystallinity of the double polymorph gamma/beta (γ/β) Ga_2O_3 structure. Thus, the data in the range of 300-400 channel numbers for $1 \times 10^{16} \text{ Ni/cm}^2$ implants correspond to the least disordered $\gamma\text{-Ga}_2\text{O}_3$ in Fig.1(a), which we adapt as a “zero” disorder level to compare with the data for higher fluences. Remarkably, the characteristic shape of the RBS/C spectra is maintained for $3 \times 10^{16} \text{ Ni/cm}^2$ and for $5 \times 10^{16} \text{ Ni/cm}^2$ implants, corresponding to 80 DPA and 132 DPA, respectively. Moreover, a minor deviation from the trend – related to an enhanced RBS/C yield – observed for the $1 \times 10^{17} \text{ Ni/cm}^2$ implants (DPA = 265), is related to an increase in the Ni content, with no significant changes in crystallinity of the surrounding matrix. It is evident from the comparison of the corresponding channelling and random spectra in Fig. 1(a) and from the STEM data in Figs. 1 (b) and (c), that the sample retains exceptionally high crystallinity even after $1 \times 10^{17} \text{ Ni/cm}^2$ implants. In fact, the SAED indexation of the sample in Fig. 1(b) confirms its identification as $\gamma\text{-Ga}_2\text{O}_3/\beta\text{-Ga}_2\text{O}_3$ double-layer structure (see SM-III). In its turn, we observed 3 – 6 nm diameter Ni precipitates embedded into the $\gamma\text{-Ga}_2\text{O}_3$ layer. These are shown in Fig. 1(c) with a magnified ADF-STEM image taken along [100] $\gamma\text{-Ga}_2\text{O}_3$ axis, resolving the precipitates in a brighter contrast (see detailed analysis in SM-IV). Additionally, the γ/β Ga_2O_3 interface exhibits stacking with rather low lattice mismatch (SM-V). Thus, based on the data in Figs. 1(a-c), $\gamma\text{-Ga}_2\text{O}_3$ tolerates up to 265 DPA without severe degradations in crystallinity of the semiconductor matrix exposed to Ni implants. This is a sensational result in particular, when compared with literature data, see the data summarized in Fig. 1(d). Indeed, as can be seen from Fig. 1(d), such materials as Si, SiC, InP have previously been shown to amorphize already at 0.2-0.5 DPA [15-17], in contrast to the

so-called high radiation tolerant materials, e.g. GaN or AlN, that are capable to accommodate much higher radiation disorder [16,18] and remaining crystalline. However, none of these materials remains such excellently crystalline as γ -Ga₂O₃, see Fig. 1(d). Notably, β -Ga₂O₃ belongs to the low radiation tolerant group of materials. However, we observe that the disorder accumulation in β -Ga₂O₃ lattice does not result in full amorphization but triggers transformation to a new crystalline polymorph [14,19-21], as illustrated with arrows showing the trend for converting the irradiated β -Ga₂O₃ volume into radiation tolerant γ -Ga₂O₃/ β -Ga₂O₃ double polymorph structure (see also SM-II). Notably, there is a gradual increase in the γ -Ga₂O₃ thickness as a function of fluence, as highlighted in Fig. 1(a) by the corresponding dashed lines. This thickness increase is consistent with our hypothesis of the disorder induced β -to- γ -Ga₂O₃ transformations [14] and the data in Fig. 1(a) may be used to estimate the corresponding disorder thresholds (see SM VI).

Further, the fact that the Ni content in Fig. 1(b-c) was sufficient for the precipitation implies that one has to account for the chemical nature of the implanted atoms, potentially altering the defect accumulation and eventual amorphization processes in γ -Ga₂O₃, as it may occur in other materials too [8]. Thus, for comparison, we investigated these phenomena for several other ions, choosing elements having strongly different chemical capabilities to interact with the matrix atoms. For that matter, Fig. 2 shows examples of the STEM data taken upon the implants resulting in the same DPA range (86-88 DPA) for Au and Ga ions. Importantly, as seen from Fig. 2(a), the same outstanding radiation tolerance of the γ -Ga₂O₃/ β -Ga₂O₃ double-layer structures is observed for the Au implants. The crystallinity of the new polymorph is confirmed by SAED patterns collected along the [100], [110], [111], [112] zone axes of γ -Ga₂O₃, shown in Fig. 2(b-e), respectively (SM-III). In contrast, for Ga ion implants we observed ~50 nm amorphous layer formed at the depth of 150-200 nm below the

surface, see Fig. 2(f). This region corresponds to the end of range for Ga ions where the concentration of implanted Ga reaches the maximum. Notably, Fig. 2(g) shows a high magnification ADF-STEM image of the interface between γ -Ga₂O₃ and amorphous phase. The corresponding FFTs in the insets of Fig. 2(g) confirm that γ -Ga₂O₃ is oriented along the [100] zone axis while the FFT in the amorphous phase shows the features that are characteristic for amorphous materials. Moreover, the difference in atomic coordination of γ -, β - and amorphous Ga₂O₃ phases is illustrated by the fine structure of the oxygen-K edge in the EELS spectra shown in Fig. 2(h). In particular, the oxygen K-edge is characterized by two peaks at 538 eV and 543 eV [22] and the relative intensity of these peaks apparently changes depending on the localization of the measurements [23], see Fig. 2(h). Importantly, lowering the Ga fluence changes the situation back to excellently maintained crystallinity in the γ -Ga₂O₃/ β -Ga₂O₃ double-layer structures. An additional cross-check with inert noble gas Ne implants confirmed the trends of this process (SM-V). Altogether, the data in Figs. 1 and 2 (plus data in Figs. S2-S8) suggest that γ -Ga₂O₃ lattice indeed tolerates unprecedentedly high values of DPA, in the order of hundreds, before it eventually breaks upon reaching even higher doses accumulating very high concentration of implanted impurities.

Importantly, these experimental observations are in excellent agreement with the results of our theoretical modelling. The high radiation tolerance of γ -Ga₂O₃ is evident from the comparison of structural modifications caused by accumulated Ga-type Frenkel pairs (FPs) in β - and γ -Ga₂O₃ (Fig. 3). We present the results obtained by classical molecular dynamics (MD) simulations of thermal equilibration of the β - and γ -Ga₂O₃ lattices with increasing number of Ga-type FPs, using the recently developed machine-learned Ga-O interatomic potential [24]. We illustrate the ordering in phases by means of radial distribution functions (RDF), i.e., pair-wise radial distributions of atoms irrespective of atom species. RDFs of crystalline structures characteristically exhibit clear peaks at the

pair distances corresponding to the coordination shells. RDFs of amorphous structures exhibit only short-range order (SRO) peaks since there is no long-range order (LRO) in these materials. For better insight, we plot the partial RDF (PRDF) within a specific atomic sublattice, i.e., the RDFs to the neighbors of a specific type (Ga-Ga, O-O or Ga-O) (see Methods). Notably, we focus on evolution of the Ga-Ga PRDF in the β - and γ -Ga₂O₃ (β - and γ -Ga PRDFs, respectively), since the Ga sublattice responds to damage evidently the strongest compared to the O-O and Ga-O PRDFs, see SM VIII, Fig. S8 for distinct differences in the Ga-Ga PRDFs and insignificant ones in the other two PRDFs with increase of number of FPs-

We show in Fig. 3a how the β - and γ -Ga PRDFs evolve with increase of the number of FPs in the series of plots up (β -Ga) and down (γ -Ga) from the pristine β - and γ -Ga PRDFs shown together in the middle. The comparison reveals a prominent feature visible only within the 2nd shell in the β -Ga PRDF (peaks at ~ 4.5 Å), which are absent in the γ -Ga PRDF (SM-VIII, Fig. S10). Apparently, this feature vanishes and a shape characteristic to the γ -Ga PRDF evolves with increasing number of FPs. The observed change manifests the β -to- γ Ga₂O₃ phase transformation with increase of Ga-type defects in β -Ga₂O₃, while similar damage level in γ -Ga₂O₃ does not result in any significant modification of the γ -Ga PRDF. Additionally Fig. 3(b) illustrates the structural differences in β -Ga₂O₃ (up) and γ -Ga₂O₃ (down) before and after introduction of 600 FPs, where the dramatic changes— compared to the initial cell—are seen only in β -Ga₂O₃ (SM VIII, Fig. S11). From quantitative comparison of the shapes of PRDFs within the 1st and the 2nd shells separately for both phases before and after introduction of Ga FPs (SM-VIII, Fig. S12), we deduce that only the damaged β -Ga PRDF within the 2nd shell underwent the most distinct shape modification. To compare these changes to the γ -Ga PRDF, we map in Fig. 3(c) the β -Ga PRDF values for the different FP numbers against the corresponding values of the pristine γ -Ga PRDF. This analysis

confirms that the shape of the damaged β -Ga PRDF with increase of Ga FPs indeed approaches that of the pristine γ -Ga PRDF. In Fig. 3(d) we plot the Pearson correlation coefficients (Pr) comparing the shapes of the β -Ga at different number of FPs with the pristine β - and γ -Ga PRDFs (violet and brown Pr curves in Fig. 3(d), respectively) versus the numbers of FPs. The comparison reveals a high degree of positive correlation (similarity) for the damaged β -Ga PRDF with that of the γ -Ga PRDF after a threshold number of FPs, at ~ 200 FPs per cell (~ 0.15 DPA) when the β -Ga₂O₃ phase inevitably transforms into γ -Ga₂O₃ phase. This is in good agreement with the experimental data (Fig. 1(d)). Moreover, we see that the FPs have only marginal effect on the γ -Ga PRDFs, as shown in Figs. 3(b) and SM Figs. S11-S12, perfectly matching the strikingly high radiation tolerance of the γ -Ga₂O₃ observed in our experiments.

To verify the insensitive response of the O-O and Ga-O sublattice to introduction of FPs observed in our MD simulations of damage accumulation, we performed dynamic single-cascade MD simulations, where the O and Ga atoms were naturally displaced in collision cascades. In these simulations, we see the O sublattice is highly rigid and strongly prone to recrystallization into face-centered-cubic (fcc) stacking, despite higher mobility of O atoms compared to Ga during the active phase of cascades, see SM-VIII, Fig. S13.

Furthermore, we study eventual chemical effects on accumulation of structural disorder in γ -Ga₂O₃ using *ab initio* MD (AIMD). Fig. 4(a) illustrates the PRDFs separately for the O-O and the heavy-ion sublattices compared to the respective initial PRDFs. The heavy-ion sublattice includes the native Ga and the added Ni, Au or Ga atoms (~ 10 at.%), while initially it includes only Ga atoms. In these simulations, the extra Ni, Ga, or Au atoms were added in random locations between the lattice sites imitating implantation of ions under high-fluence irradiation. After that the structures were

thermally equilibrated using AIMD to obtain the most energetically favourable structures (more data in SM VIII, Figs. S14-S15). Since the presence of LRO peaks in an RDF can be used as a crystallinity measure, we analyse both the O-O and heavy ion PRDF fluctuations around the unity (grey dotted line at $g(r)=1$ in Fig. 4(a)) beyond the SRO peaks separated by the vertical grey dotted lines at distances 3.6 Å and 4.0 Å for the O-O and the heavy ions pairs, respectively. In Fig. 4b we quantify the degree of amorphization in the lattices with the implanted ions by integrating the total deviation area of the PRDF curves from the dotted lines ($g(r) = 1$) beyond the SRO peaks in Fig. 4(a) by the vertical grey dotted lines. The smaller the deviation area the higher the degree of amorphization the structure exhibits. Naturally, the PRDFs of the stoichiometric $\gamma\text{-Ga}_2\text{O}_3$ with multiple peaks and valleys along the $g(r)=1$ line has the largest deviation area. Remarkably, the strongest disordering effect of the implanted atoms – the smallest deviation area – is observed in the cell with the Ga excess, which in an excellent agreement with the experiments (Fig. 2). However, the deviation area for the Ga-Au/Ga PRDF is only marginally larger than that of the Ga-Ga/Ga PRDF. Hence, we further analyse the disorder in the implanted lattices by comparing the bond-angle distributions for the O-O bonds for all three distorted structures with the pristine one in Fig. 4(c) and the Pr similarity analysis in Fig. 4(d). The visual inspection of the plots in Fig. 4(c) reveals that the O-O bond angle peaks of the pristine lattice coincide with those of the Ni (green) and Au (golden) implanted structures, while the Ga-implanted cell does not exhibit similar O-O fcc bond-angle peaks beyond the first one at $\sim 60^\circ$. Consistently, the Pr coefficients for the O-O bond-angle distributions in the Ni- and Au-implanted structures are close to the unity, which shows high degree of similarity with the corresponding distribution in the pristine $\gamma\text{-Ga}_2\text{O}_3$. In contrast, for the Ga-implanted structure Pr is only ~ 0.5 , which essentially indicates the amorphization. This fact may be readily interconnected with the disturbance in the ionic charge distribution (charge

transfer from the excess Ga atoms to the closest O ions) affecting the Columbic interaction that maintains the order in an ionic system. Moreover, in Fig. 4a we see additional peaks in the green (Ni) and the purple (Ga) heavy-ion PRDF curves at 2.5 Å and 2.7 Å, respectively. These peaks can be correlated with metallic Ni precipitates observed in Fig. 1, while the Ga-Ga bonds may contribute to amorphization of the layer with the highest concentration of Ga ions in the Ga-implanted Ga₂O₃ in Fig. 2.

In conclusion, the full set of the experimental and theoretical data in Figs. 1-4 may be seen as solid evidence for a discovery of the outstanding radiation tolerance in the γ -Ga₂O₃/β-Ga₂O₃ double-polymorph structures, practically independent of DPA. Meanwhile, the chemical effect introduced by high-dose Ga ions leads to a nonstoichiometric disordered layer. This observation is rationalized by the unique combination of the specific features of both γ -Ga and O sublattices of γ -Ga₂O₃. Intrinsically defective, the γ -Ga sublattice is nearly insensitive to new point defects produced in collision cascades during ion irradiation, while the O sublattice is prone to rapid post-cascade recrystallization into original fcc stacking. The collaborative effect of both features explains macroscopically negligible structural deformations observed in heavily irradiated γ -Ga₂O₃.

Methods

We used commercial (010) monoclinic beta Ga_2O_3 polymorph ($\beta\text{-Ga}_2\text{O}_3$) single crystals wafers from Tamura Corporation as initial polymorph substrates. To start with the samples were converted to double Ga_2O_3 polymorph structures with the implantation parameters as reported in Ref. 14. For that matter we used $^{58}\text{Ni}^+$, $^{69}\text{Ga}^+$, $^{197}\text{Au}^+$ and $^{20}\text{Ne}^+$ ion implantation at room temperature, in particular adjusting implantation energies and fluences to obtain double polymorph Ga_2O_3 structures of comparative thickness while using different ions. Notably, all implants were performed at 7° off the normal direction of the wafer to minimize channeling. Table I summarizes the implantation parameters used in the experiments. Notably, the maximum of the nuclear energy loss profile (R_{pd}), the projected range (R_p) as well as the DPA values for each ion were calculated using the SRIM code [25] simulations (see SM-I). Table I also shows the ion fluences corresponding to 1 DPA in order to facilitate the fluence/DPA conversion for the readers. Importantly, upon each fluence collection step, the samples were measured by the Rutherford backscattering spectrometry in channeling mode (RBS/C), while selected samples were also characterized with the scanning transmission electron microscopy (STEM).

Ion	Energy (keV)	Fluence			R_{pd} (nm)	R_p (nm)	Max conc. (at.%)
		(ions/cm ²)	1 DPA (ions/cm ²)	(DPA)			
$^{58}\text{Ni}^+$	400	$2 \times 10^{13} - 1 \times 10^{17}$	3.8×10^{14}	0.05-265	115	160	0.001-5.8
$^{197}\text{Au}^+$	1200	$3 \times 10^{15}, 1 \times 10^{16}$	1.2×10^{14}	26, 86	110	160	0.3, 0.9
$^{69}\text{Ga}^+$	500	$1 \times 10^{16}, 3 \times 10^{16}$	3.5×10^{14}	29, 88	125	190	0.6, 1.9
$^{20}\text{Ne}^+$	140	3.5×10^{16}	1.3×10^{15}	26	118	170	2.2

Table I. Implantation parameters used in the present study.

The RBS/C measurements were performed using 1.6 MeV He^+ ions incident along [010] $\beta\text{-Ga}_2\text{O}_3$ direction and 165° backscattering geometry. Importantly, it is known from literature that upon the double polymorph Ga_2O_3 structure formation, the RBS/C yield exhibits a characteristic trend, attributed to the channeling conditions in the newly formed gamma Ga_2O_3 polymorph ($\gamma\text{-Ga}_2\text{O}_3$) film - see SM-II for more details. This trend, if maintained as a function of the further fluence accumulation, is a fingerprint of the maintained crystallinity. Moreover, the horizontal scale in the RBS/C plots – the channel number – measures the thickness of the newly formed polymorph. Notably, Ga-parts of the RBS/C data were used in the analysis because of significantly higher sensitivity of this method for heavier Ga-sublattice comparing to the O-sublattice.

Further, STEM was used for detailed crystal structure and chemical analysis. For cross-sectional STEM studies, selected samples were thinned by mechanical polishing and by Ar ion milling in a Gatan PIPS II (Model 695), followed by plasma cleaning (Fishione Model 1020) immediately before loading the samples into microscope. High Resolution Scanning Transmission Microscopy (HRSTEM) imaging, selected area electron diffraction (SAED), energy dispersive x-ray spectroscopy (EDS), and electron energy-loss spectroscopy (EELS) measurements were done at 300 kV in a Cs-corrected Thermo Fisher Scientific Titan G2 60-300 kV microscope, equipped with a Gatan GIF Quantum 965 spectrometer and Super-X EDS detectors. The STEM images were recorded using a probe convergence semi-angle of 23 mrad, a nominal camera length of 60 mm using three different detectors: high-angle annular dark field (HAADF) (collection angles 100–200 mrad), annular dark field (ADF) (collection angles 22–100 mrad) and bright field (BF) (collection angles 0–22 mrad). The structural model of both phases was displayed using VESTA software [26].

EBSD was performed on the Ne irradiated sample in a Zeiss NVision 40 scanning

electron microscope (SEM) equipped with a field emission electron cathode and a Bruker EBSD system with an e-Flash HR+ detector. To ensure the removal of a possible carbon contamination layer, the sample was cleaned for 45 seconds in an air plasma cleaner. The acceleration voltage was set to 30 kV, the beam current to about 10 nA using a 120 μm aperture. In order to record low noise high quality EBSD patterns, the detector resolution was set to 800×570 pixels and the exposure time to 8×122 ms per frame. EBSD was done as mappings of 20×15 steps, with a step size of 1.9 μm on the irradiated and the unirradiated surface sections of the sample

The *ab initio* molecular dynamics (AIMD) simulations were conducted using the Vienna Ab-initio Simulation Package (VASP) [27], employing the projected augmented-wave method [28]. The Perdew-Burke-Ernzerhof version of the generalized gradient approximation was used as exchange-correlation functional [29]. The electronic states were expanded in plane-wave basis sets with an energy cutoff of 400 eV throughout all AIMD runs. The Brillouin zones were sampled with a single- Γ k -point for a $1 \times 2 \times 4$ 160-atom $\beta\text{-Ga}_2\text{O}_3$ supercell, and a Γ -centered $2 \times 2 \times 1$ k -mesh for a $1 \times 1 \times 3$ 160-atom $\gamma\text{-Ga}_2\text{O}_3$ supercell. In these simulations, the increase of experimental fluence was mimicked by introducing implanted atoms (Ni, Au, or Ga) in interstitial and substitutional (specified by the superscript S) lattice sites. Specifically, we added 8, 12 and 16 atoms of a given species, which corresponded to 5 at.%, 7.5 at.% and 10 at.% concentrations with respect to the initial number of atoms in the cell. Initially, the obtained structures were relaxed to the local energy minimum with and without constraining the volume of the cell. Then, the relaxed cells were used in AIMD simulations to enable dynamic evolution of the system to accommodate the added atoms in the best possible configurations. These simulations were performed for 5 ps with the step of 2 fs in isothermal-isobaric ensemble [30] at 900 K and 1 bar, employing Langevin thermo- and barostats [31].

The large-scale classical MD simulations were conducted using LAMMPS package [32]. The newly developed machine-learning interatomic potential of Ga_2O_3 system was employed [24]. The potential is developed to guarantee the high accuracy for $\beta/\kappa/\alpha/\delta/\gamma$ polymorphs and universal generality for disordered structures. In these simulations, Ga Frenkel pairs (FPs) were generated cumulatively in 1280-atom $\beta\text{-Ga}_2\text{O}_3$ and a 1440-atom $\gamma\text{-Ga}_2\text{O}_3$ cells by iteratively displacing a random Ga atom following a randomly directed vector with norm of 10~15 Å. The two systems then firstly were relaxed to the local minimum to avoid initial atom overlapping and secondly were thermalized with *NPT*-MD for 5 ps at 300 K and 0 bar. In total, 600 Ga-FP iterations were run for both cells. In addition, we have performed MD simulations of single cascades in $\beta\text{-Ga}_2\text{O}_3$ at 300K. The initial momentum direction and the position of a primary knock-on atom (PKA) were selected randomly at the center of the simulation cell. The PKA was assigned the kinetic energy of 1.5 keV. Periodic boundary conditions were applied in all directions. The temperature was controlled using a Nosé-Hoover thermostat [33] only at the borders of the simulation cell to imitate the heat dissipation in bulk materials. To avoid the cascade overlap with temperature-controlled borders, the number of atoms in the simulation cell was increased to 160 000. We applied the adaptive time step [34] for efficiency of MD simulations in the active cascade phase. Electronic stopping as a friction term was applied to the atoms with kinetic energies above 10 eV. The simulation time of the single cascades was 50 ps. 120 simulations with different PKA were carried out for statistical analysis.

The structural modifications due to accumulated damage in the studied lattices were analyzed using radial distribution functions. The radial distribution function (RDF) is defined as the ratio of the ensemble-average local number density of particles, $\langle\rho(r)\rangle$, at a distance r from a reference particle to the average number density of particles in system.

$$g(r) = \frac{\langle \rho(r) \rangle}{N_{at.}/V},$$

where $N_{at.}$ is the total number of particles, and V is the system cell volume. Essentially, the RDF is a fingerprint descriptor of the structural property of a system of particles down atomic scale. For a crystal structure this function is characterized by well pronounced peaks at the radial distances corresponding the radii of coordination shells. While the short-range order (SRO) peaks are practically always present in a structure, the long-range order (LRO) peaks in amorphous structures are indistinguishable, since the number density of the atoms in the spherical shells at long distances in an amorphous structure is the same as the average number density in the structure. This feature of RDF gives good measure of crystallinity in the studied structures.

The partial RDF (PRDF) describes the type-specified sublattice in a multi-species system [35]. We performed a detailed analysis of the Ga-Ga, Ga-O and O-O PRDFs as a function of stochastically generated FPs. All RDF distributions were obtained by averaging the signals between 2 to 5 ps for the frames recorded at every simulation step. For clarity, we discriminated the Ga-Ga PRDF features within so-called 1st and 2nd shells. The division was based on significance of changes that are observed in PRDF distributions before and after the damage accumulation. The border was selected at the valley at $\sim 4.0\text{\AA}$. The Pearson correlation coefficient, Pr , between any two given curves is calculated with the formula:

$$Pr = \frac{\sum_{i=1}^n (A_i - \bar{A})(B_i - \bar{B})}{\sqrt{\left[\sum_{i=1}^n (A_i - \bar{A})^2\right] \left[\sum_{i=1}^n (B_i - \bar{B})^2\right]}}$$

where A_i and B_i are the variable samples of the two curves, respectively, and \bar{A} and \bar{B} are the mean values of the variable samples, respectively.

Competing Interests

The authors declare no competing interests.

Additional information

Supplementary information is available for this paper at ...

Correspondence and requests for materials should be addressed to A.A. and A.K.

Data availability

“The datasets generated during and/or analysed during the current study are available from the corresponding author on reasonable request”

Author contribution

A.K. and A.A. conceived the research strategy and designed the methodological complementarities. A.A., J.G.F., U.B., P.C., and N.K carried out experiments and provided initial drafts for the description of the experimental data. H.H., H.R., and J.Z performed molecular dynamics simulations. F.D. and J.Z. developed the theoretical models and composed the theoretical part of the manuscript. A.K. and A.A. finalized the manuscript with the input from all the co-authors. All co-authors discussed the results as well as reviewed and approved the manuscript. A.K., L.V., Ø.P., F.D, and G.H. administrated their parts of the project and contributed to the funding acquisition. A.K. coordinated the work of the partners.

Acknowledgements

M-ERA.NET Program is acknowledged for financial support via GOFIB project (administrated by the Research Council of Norway project number 337627 in Norway, the Academy of Finland project number 352518 in Finland, and the tax funds on the basis of the budget passed by the Saxon state parliament in Germany). The experimental infrastructures were provided at the Norwegian Micro- and Nano-Fabrication Facility, NorFab, supported by the Research Council of Norway project number 295864, at the Norwegian Centre for Transmission Electron Microscopy, NORTEM, supported by the Research Council of Norway project number 324563. Support from the Ion Beam Center at the HZDR is acknowledged too. Computing resources were provided by the Finnish IT Center for Science (CSC) and by the Center for Computational Science and Engineering at the Southern University of Science and Technology. The computational work was also partially supported by Guangdong Basic and Applied Basic Research Foundation under Grant 2023A1515012048. The international collaboration was also fertilized via the COST Action FIT4NANO CA19140, supported by COST (European Cooperation in Science and Technology, <https://www.cost.eu/>), and via INTPART Program at the Research Council of Norway project number 322382.

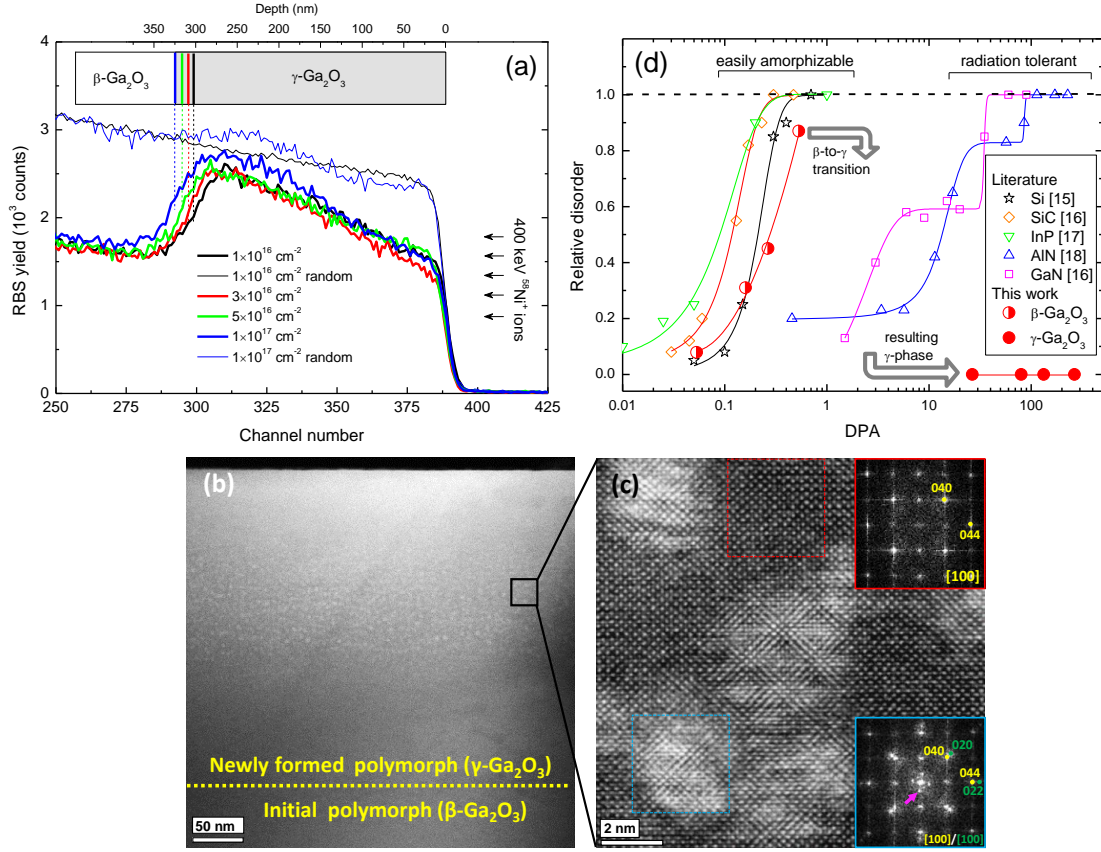


Figure 1. High radiation tolerance of the double γ -Ga₂O₃/β-Ga₂O₃ polymorph structures. (a) RBS/C spectra of β-Ga₂O₃ samples implanted with 400 keV ⁵⁸Ni⁺ ions to the different doses as indicated in the legend. (b) low magnification HAADF-STEM image of the 1×10¹⁷ Ni/cm² sample showing full implanted region, (c) high resolution ADF-TEM and corresponding FFTs of the areas with (blue) and without (red) Ni precipitates. γ-Ga₂O₃ planes are indicated in yellow, metallic Ni in green and double diffraction spots are indicated with a pink arrow; (d) relative disorder as a function of DPA for easily amorphizable (Si [15], SiC [16] and InP [17]) and radiation tolerant semiconductors (GaN [16], and AlN [18]) for Au implants at room temperature, as well as for Ga₂O₃ (this work) - the lines are a guide to the eye. Notably, the depth scale in panel (a) is calculated for Ga atoms, so that the Ni related peak appears deeper in the sample (see SM-II for clarity).

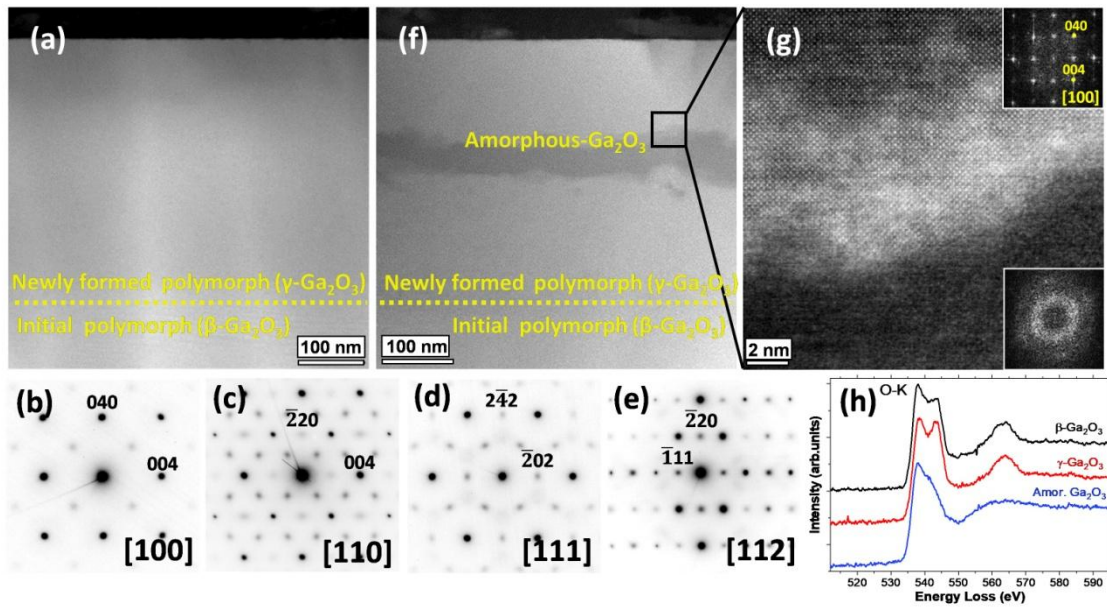


Figure 2. **Role of ion species in the radiation tolerance of γ -Ga₂O₃.** Low magnification HAADF-STEM images of the samples implanted with (a) Au and (f) Ga ions with the doses corresponding to the 86-88 DPA range. SAED patterns of the γ -layer taken along [100], [110], [111] and [112] directions in the Au implanted sample are shown in the panels (b), (c), (d) and (e) respectively. (g) High Resolution ADF-TEM image of the Ga implanted sample taken at the amorphous/crystalline interface with corresponding FFTs. (h) EELS spectra of the oxygen-K edge, acquired from β -, γ - and amorphous Ga₂O₃ phases.

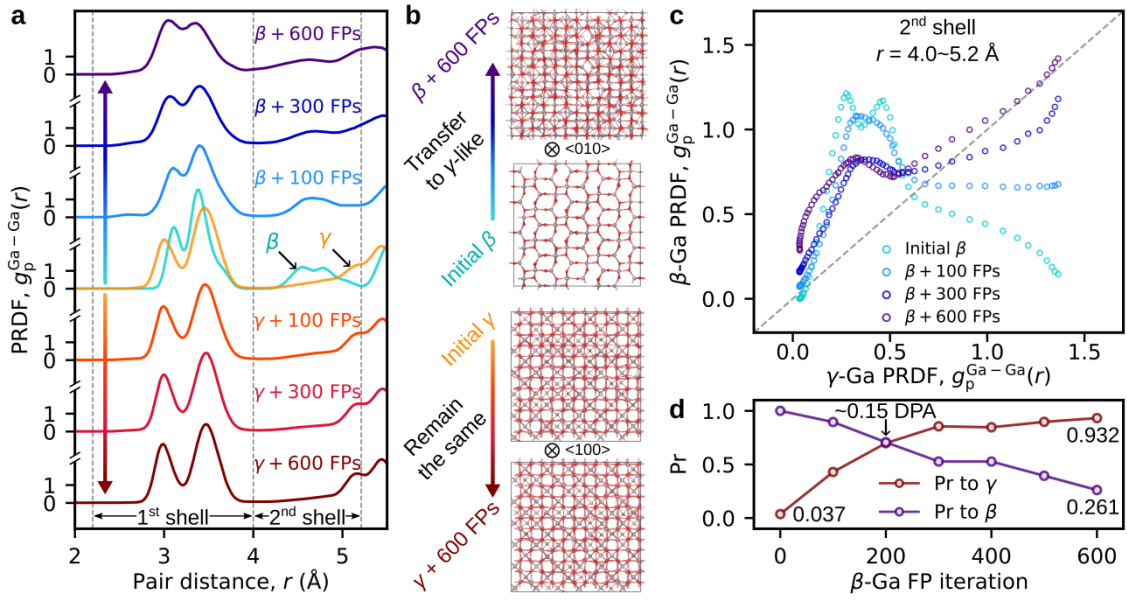


Figure 3. **Analysis of the PRDFs of Ga sublattices with additional Ga FPs in Ga_2O_3 lattices:** (a) Ga-Ga PRDFs for the pristine β - and γ - Ga_2O_3 lattices (in the middle); up and down from the pristine Ga-Ga PRDFs, the same PRDFs for the lattices with increasing numbers of FPs (up for β - Ga_2O_3 and down for γ - Ga_2O_3). For the analysis of structural modifications, the features of the Ga-Ga PRDFs are considered separately within the 1st (2.2–4.0 Å) and 2nd (4.0–5.2 Å) shells that are indicated by the vertical thin dashed lines. (b) The snapshots show modifications of both the β - Ga_2O_3 (up) and the γ - Ga_2O_3 (down) from the pristine lattices to the lattices with added 600 FPs. Ga ions are shown in brown and O in red. (c) The increasing similarity of the PRDF values of the β -Ga sublattice with increasing number of FPs versus the PRDF of the pristine γ -Ga within the 2nd shell. (d) The Pearson correlation coefficient, Pr , calculated within the 2nd shell for the PRDF of the increasingly damaged β -Ga with respect to the pristine β -Ga and γ -Ga PRDFs as a function of the FP number. The similarity to the γ -Ga phase is stronger above the threshold number of FPs (~ 200) compared to the similarity to the original β -Ga sublattice. See SM-VIII Fig. S9-S12 for more details.

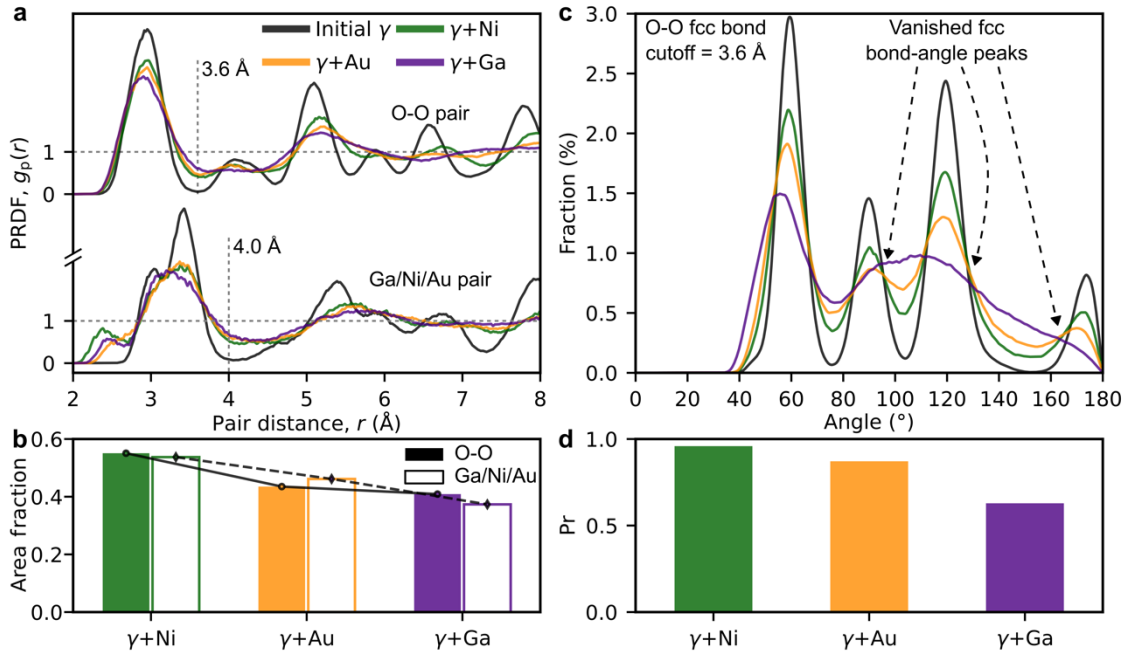


Figure 4. Chemical effect of the foreign ions on the disordering of γ - Ga_2O_3 lattice: (a) AIMD-PRDFs of O-O and heavy-ion (Ga/Ni/Au) pairs at 900 K and 0 bar. The first valleys are at 3.6 and 4.0 Å, as labelled by the vertical dashed lines. (b) Ratios of the absolute areas (covered by the PRDF curves with reference to 1) of the distorted cells against the initial γ cell. (c) Bond angle distribution of O sublattice with O-O bond cutoff at 3.6 Å. (d) The Pr values of the distorted bond-angle distribution to the one of the initial γ cell. See SM-VIII Fig. S14-S15 for more details.

References:

- 1 J. S. Williams, “Ion implantation of semiconductors”, *Mater. Sci. Eng. A* **253**, 8 (1998).
- 2 E. Wendler, “Mechanisms of damage formation in semiconductors”, *Nucl. Instrum. Methods Phys. Res. B* **267**, 2680 (2009).
- 3 K. E. Sickafus, L. Minervini, R. W. Grimes, J. A. Valdez, M. Ishimaru, F. Li, K. J. McClellan, and T. Hartmann, “Radiation tolerance of complex oxides”, *Science* **289**, 748 (2000).
- 4 Y. Zhang and W. J. Weber, “Ion irradiation and modification: The role of coupled electronic and nuclear energy dissipation and subsequent nonequilibrium processes in materials”, *Appl. Phys. Rev.* **7**, 041307 (2020).
- 5 D. R. Pereira, C. Díaz-Guerra, M. Peres, S. Magalhães, J. G. Correia, J. G. Marques, A. G. Silva, E. Alves, and K. Lorenz, “Engineering strain and conductivity of MoO₃ by ion implantation”, *Acta Mater.* **169**, 15 (2019).
- 6 A. Debelle, A. Boule, A. Chartier, F. Gao, and W. J. Weber, “Interplay between atomic disorder, lattice swelling, and defect energy in ion-irradiation-induced amorphization of SiC”, *Phys. Rev. B.* **90**, 174112 (2014).
- 7 A. Yu. Azarov, A. Hallén, P. Rauwel, X. L. Du, A. Yu. Kuznetsov, and B. G. Svensson, “Effect of implanted species on thermal evolution of ion-induced defects in ZnO”, *J. Appl. Phys.* **115**, 073512 (2014).
- 8 S. O. Kucheyev, J. S. Williams, and C. Jagadish, J. Zou, and G. Li, “Damage buildup in GaN under ion bombardment”, *Phys. Rev. B.* **62**, 7510 (2000).
- 9 J. Y. Tsao, S. Chowdhury, M. A. Hollis, D. Jena, N. M. Johnson, K. A. Jones, R. J. Kaplar, S. Rajan, C. G. Van de Walle, E. Bellotti, C. L. Chua, R. Collazo, M.

- E. Coltrin, J. A. Cooper, K. R. Evans, S. Graham, T. A. Grotjohn, E. R. Heller, M. Higashiwaki, M. S. Islam, P. W. Juodawlkis, M. A. Khan, A. D. Koehler, J. H. Leach, U. K. Mishra, R. J. Nemanich, R. C. N. Pilawa-Podgurski, J. B. Shealy, Z. Sitar, M. J. Tadjer, A. F. Witulski, M. Wraback, and J. A. Simmons, “Ultrawide-bandgap semiconductors: Research opportunities and challenges”, *Adv. Electron. Mater.* **4**, 1600501 (2018).
- 10 S. J. Pearton, J. Yang, P. H. Cary IV, F. Ren, J. Kim, M. J. Tadjer, and M. A. Mastro, “A review of Ga_2O_3 materials, processing, and devices”, *Appl. Phys. Rev.* **5**, 011301 (2018).
 - 11 M. J. Tadjer, “Toward gallium oxide power electronics”, *Science* **378**, 724 (2022).
 - 12 J. Kim, S. J. Pearton, C. Fares, J. Yang, F. Ren, S. Kim, and A. Y. Polyakov, “Radiation damage effects in Ga_2O_3 materials and devices”, *J. Mater. Chem. C* **7**, 10 (2019).
 - 13 Playford, H. Y., Hannon, A. C., Barney, E. R. and Walton, R. I. Structures of uncharacterised polymorphs of gallium oxide from total neutron diffraction. *Chem.-A Eur. J.* **19**, 2803-2813 (2013).
 - 14 A. Azarov, C. Bazioti, V. Venkatachalapathy, P. Vajeeston, E. Monakhov, and A. Kuznetsov, “Disorder-induced ordering in gallium oxide polymorphs”, *Phys. Rev. Lett.* **128**, 015704 (2022).
 - 15 J. C. Cheang-Wong, A. Crespo-Sosa, and A. Oliver, “RBS-channeling studies on damage production by MeV ion implantation in Si(111) wafers”, *Mater. Sci. Eng. B* **84**, 205 (2001).
 - 16 W. Jiang, W. J. Weber, and S. Thevuthasan, “Ion implantation and thermal annealing in silicon carbide and gallium nitride”, *Nucl. Instrum. and Methods in*

- Phys. Res. B **178**, 204 (2001).
- 17 A. S. Khalil and A. Yu. Didyk, “RBS and TEM studies of indium phosphide irradiated with 100 keV Au ions”, Phys. Part. Nucl. Lett. **6**, 498 (2009).
 - 18 S. O. Kucheyev, J. S. Williams, J. Zou, C. Jagadish, M. Pophristic, S. Guo, I. T. Ferguson, and M. O. Manasreh, “Ion-beam-produced damage and its stability in AlN films”, J. Appl. Phys. **92**, 3554 (2002).
 - 19 E. A. Anber, D. Foley, A. C. Lang, J. Nathaniel, J. L. Hart, M. J. Tadjer, K. D. Hobart, S. Pearton, and M. L. Taheri, “Structural transition and recovery of Ge implanted β -Ga₂O₃”, Appl. Phys. Lett. **117**, 152101 (2020).
 - 20 T. Yoo, X. Xia, F. Ren, A. Jacobs, M. J. Tadjer, S. Pearton, and H. Kim, “Atomic-scale characterization of structural damage and recovery in Sn ion-implanted β -Ga₂O₃”, Appl. Phys. Lett. **121**, 072111 (2022).
 - 21 J. García-Fernández, S. B. Kjeldby, P. D. Nguyen, O. B. Karlsen, L. Vines, and III. Prytz, ” Formation of γ -Ga₂O₃ by ion implantation: Polymorphic phase transformation of β -Ga₂O₃” Appl. Phys. Lett. **121**, 191601 (2022).
 - 22 A. Sharma, M. Varshney, H.-J. Shin, K. H. Chae, and S. O. Won, “Investigation on cation distribution and luminescence in spinel phase γ -Ga_{3- δ} O₄: Sm nanostructures using X-ray absorption spectroscopy”, RSC Adv. **7**, 52543 (2017).
 - 23 L. Shang, Y. Wang, M. Zhuang, B. Liu and F. Shi, “Growth behavior of β -Ga₂O₃ nanowires synthesized by chemical vapor deposition”, Mater. Res. Express **6**, 1150a5, (2019).
 - 24 J. Zhao, J. Byggmästar, H. He, K. Nordlund, F. Djurabekova, and M. Hua, “Complex Ga₂O₃ polymorphs explored by accurate and general-purpose

- machine-learning interatomic potentials”, <https://arxiv.org/abs/2212.03096>
- 25 J. F. Ziegler, M. D. Ziegler, and J. P. Biersack, “SRIM—the stopping and range of ions in matter (2010)”, Nucl. Instrum. Methods Phys. Res. B **268**, 1818 (2010).
 - 26 K. Momma and F. Izumi, “VESTA 3 for three-dimensional visualization of crystal, volumetric and morphology data,” J. Appl. Crystallogr. **44**, 1272 (2011).
 - 27 G. Kresse and J. Furthmüller, “Efficiency of ab-initio total energy calculations for metals and semiconductors using a plane-wave basis set”, Comput. Mater. Sci. **6**, 15–50 (1996).
 - 28 P. E. Blöchl, “Projector augmented-wave method”, Phys. Rev. B **50**, 17953 (1994).
 - 29 J. P. Perdew, K. Burke, and M. Ernzerhof, “Generalized gradient approximation made simple”, Phys. Rev. Lett. **77**, 3865 (1996).
 - 30 M. Parrinello and A. Rahman, “Crystal Structure and Pair Potentials: A Molecular-Dynamics Study”, Phys. Rev. Lett. **45**, 1196 (1980).
 - 31 T. Schneider and E. Stoll, “Molecular-dynamics study of a three-dimensional one-component model for distortive phase transitions”, Phys. Rev. B **17**, 1302 (1978).
 - 32 S. Plimpton, “Fast Parallel Algorithms for Short-Range Molecular Dynamics”, J. Comput. Phys. **117**, 1 (1995).
 - 33 S. Nosé, “A molecular dynamics method for simulations in the canonical ensemble”, Mol. Phys. **100**, 191 (2002).
 - 34 K. Nordlund, “Molecular dynamics simulation of ion ranges in the 1–100 keV energy range”, Comput. Mater. Sci. **3**, 448(1995).

- 35 J. L. Yarnell, M. J. Katz, R. G. Wenzel, and S. H. Koenig, “Structure factor and radial distribution function for liquid argon at 85 K”, *Phys. Rev. A* **7**, 2130 (1973).

Supplementary Materials for

Universal radiation tolerant semiconductor

Alexander Azarov¹, Javier García Fernández¹, Junlei Zhao², Flyura Djurabekova³, Huan He³, Ru He³, Øystein Prytz¹, Lasse Vines¹, Umutcan Bektas⁴, Paul Chekhonin⁴, Nico Klingner⁴, Gregor Hlawacek⁴ and Andrej Kuznetsov¹

¹ *University of Oslo, Centre for Materials Science and Nanotechnology, PO Box 1048 Blindern, N-0316 Oslo, Norway*

² *Department of Electrical and Electronic Engineering, Southern University of Science and Technology, Shenzhen 518055, China*

³ *Department of Physics, University of Helsinki, P.O. Box 43, FI-00014 Helsinki, Finland*

⁴ *Helmholtz-Zentrum Dresden-Rossendorf, D-01328 Dresden, Germany*

Table of Contents

I.	DPA calculations and implant parameters normalization	28
II.	Explanation of the RBS/C data for extraction of relative disorder in β - and γ -Ga ₂ O ₃	30
III.	Identification of the newly formed polymorph γ -Ga ₂ O ₃	32
IV.	Formation of metallic Ni precipitates	33
V.	Low mismatch interface stacking in γ/β -Ga ₂ O ₃ double polymorph structures obtained by ion irradiation	34
VI.	Defect balance at the β/γ -Ga ₂ O ₃ interface	37
VII.	Impact of Ga sub-lattice non-stoichiometry on the radiation tolerance in γ -Ga ₂ O ₃	39
VIII.	Additional details of computational modelling	40
	References	46

I. DPA calculations and implant parameters normalization

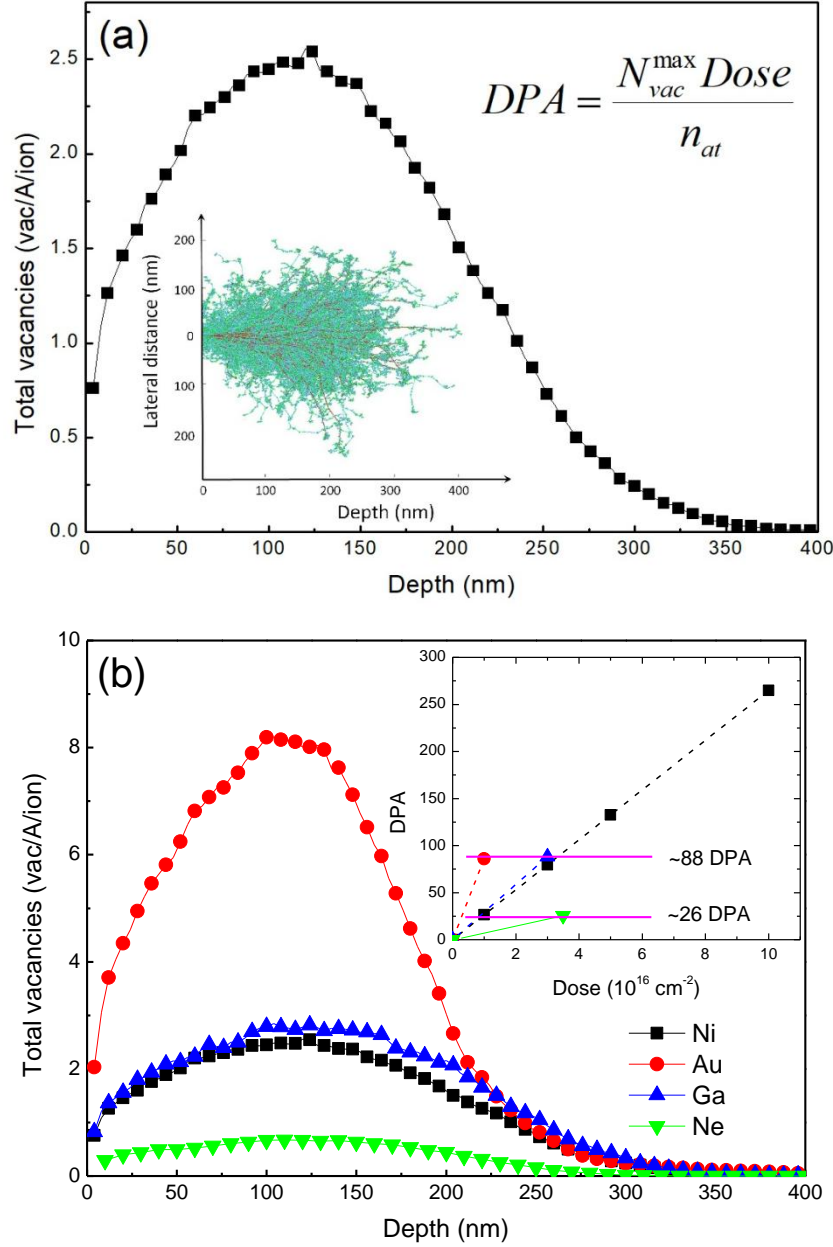


Fig. S1. (a) Schematic illustration of DPA calculation using SRIM. (b) Depth profiles of the total vacancies per implanted ion as calculated using SRIM for Ne, Ni, Ga and Au ions. The inset shows the DPA value taken in the maximum of the defect profiles as a function of the implanted dose for the all implants used in the present study.

Here we use a conventional methodology of DPA calculation (see, for example, [S1]. Figure S1(a) illustrates the DPA calculation procedure. Initially, the depth profiles of ion generated vacancies were calculated using SRIM code [S2] simulations in a full cascade mode as illustrated in Fig. 1(a) for 400 keV Ni implants. The inset in Fig. 1(a) shows a spatial distribution of primary defects (dots) obtained using the SRIM code simulations for 300 ion impacts. The SRIM calculations were performed with 25 eV and 28 eV as the displacement energies for Ga and O atoms, respectively. The DPA

values are taken from the depth corresponding to the highest magnitude in the SRIM vacancy generation profiles ($N_{\text{vac}}^{\text{max}}$) for a given fluence (*dose*), normalized to an atomic density of $\beta\text{-Ga}_2\text{O}_3$ ($n_{\text{at}} = 9.45 \times 10^{22} \text{ at/cm}^3$) (see the equation in Fig. 1(a)). Note that the atomic density of $\gamma\text{-Ga}_2\text{O}_3$ is close to that of β -phase ($n_{\text{at}} = 9.54 \times 10^{22} \text{ at/cm}^3$) [S3], so that the obtained DPA values can be used for both polymorphs.

The implantation parameters of Ne, Ga and Au ions were adjusted in such a way that they resulted in similar absolute numbers and distributions of primary defects. In order to illustrate this normalization, the SRIM calculated depth profiles of total generated lattice vacancies as a function of depth are plotted in Fig. 1(b) for all four ions studied. It is seen that all the defect generation profiles have a similar shape with the R_{pd} is in the range of 110-120 nm (see also Table I in the main text). It is seen that Ga and Ni ions produce nearly the same number of primary defects since the atomic masses of these atoms are close to each other. In its turn, Au ions generate denser collision cascades containing more defects, as compared to both Ga and Ni ions, by a factor of 3, while Ne ions generate less defects as compared by Ni ones by a factor of 3.5. The inset in Fig. S1(b) shows the calculated DPA values as a function of the dose for all four ions used in the present study. The solid lines in the inset indicates the implantation doses for all the ions corresponding to the similar DPA values of ~ 88 and ~ 26 , which were used for the additional Ne, Ga and Au implantations.

II. Explanation of the RBS/C data for extraction of relative disorder in β - and γ -Ga₂O₃.

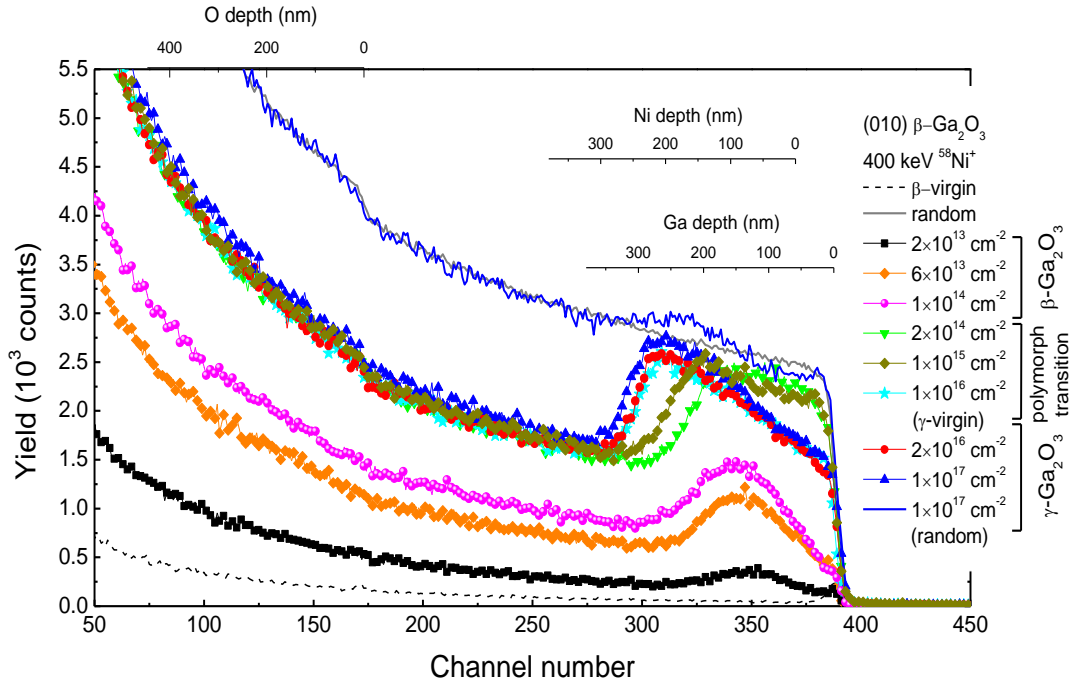


Fig. S2. RBS/C spectra of (010) β -Ga₂O₃ samples implanted with 400 keV $^{58}\text{Ni}^+$ ions for different fluencies as indicated in the legend. The channeling spectrum of the unimplanted (β -virgin) sample is shown by a dashed line for a comparison. Spectra acquired for the random incidence of the He beam are shown too.

Fig. S2 shows full-scale RBS/C spectra of Ni implanted β -Ga₂O₃ samples for different fluencies. The labeled Ga, Ni and O depth scales are included in the figure with the surface position corresponding to channel numbers at 386, 370 and 172, respectively. It should be noted that the sensitivity of the RBS technique depends on the atomic mass of the elements comprising the target, so that it is more sensitive to Ga atoms as compared to O atoms. Thus, only the Ga parts of the RBS/C data are used and discussed below as it is also done in the main text.

As seen from Fig. S2 for the low fluences (2×10^{13} – $1 \times 10^{14} \text{ Ni/cm}^2$) the RBS/C spectra form a well-defined disorder peak visible on the Ga sublattice centered around the maximum of the nuclear energy loss profile - R_{pd} (see Table I). The increase of the fluence up to $2 \times 10^{14} \text{ Ni/cm}^2$ leads to the formation of the “box-like” disorder profile extending up to 180 nm from the surface. The disorder level in this layer does not reach the random level confirming that β -Ga₂O₃ is not fully amorphous state. Further fluence increase up to $1 \times 10^{15} \text{ Ni/cm}^2$ leads to the broadening of this “box-like” disorder profile into the bulk of the sample with nearly maintained amplitude of the disorder level. Prominently, the increase of the fluence to $1 \times 10^{16} \text{ Ni/cm}^2$ leads to further broadening

into the bulk and a remarkable decrease in the RBS/C yield of the feature we called “box-like disorder” above. Recently, Azarov *et. al.* [14] demonstrated that this evolution is attributed to the disorder-induced phase transformations in the implanted region, so that a double polymorphic structure forms. Following Ref. [14], we associate the (2×10^{14} - 1×10^{16} Ni/cm²) fluence range to the polymorph transition (see “polymorph transition” label in Fig. S2 and the arrow in Fig. 1(d)).

Notably, even though early works [14,19] identified this new polymorph as kappa-phase, now, it is established that it maintains γ -phase symmetry, independently of the ion type used in the implants [21,20], fully consistently with our observations/interpretations in this work. Moreover, according to the literature [14,21,20] and the STEM data in the present work (SM-III and SM-VII) this γ -Ga₂O₃ exhibits high crystallinity. Thus, for Figs.1 and S2 we consider the γ -Ga₂O₃ part of the double γ/β polymorph structure formed with 1×10^{16} Ni/cm², as a “virgin γ -Ga₂O₃” to which we may interrelate disorder changes eventually occurring for higher fluences. Notably, the absolute RBS/C yield for this “virgin γ -Ga₂O₃” spectrum is significantly higher than that for the initial “virgin β -Ga₂O₃”. This is not a consequence of a poor crystallinity. It is because the alignment for the experiments in Figs. 1 and S2 was done along the (010) direction in the β -Ga₂O₃, which is not main channel in γ -Ga₂O₃, according to the orientation relationship at the γ/β interface as measured in SM-V.

Thus, for Fig. 1(d) we calculate the relative disorder in β -Ga₂O₃ implanted with low fluences (2×10^{13} - 1×10^{14} Ni/cm²) using one of the conventional algorithms [S19] obtaining the data ranging from 0 to 1 corresponding to the perfect and amorphous materials, respectively. In its turn, the relative disorder in γ -Ga₂O₃, eventually happening in the course of the high dose accumulation, can be estimated by the deviations of the corresponding RBS/C amplitudes from that we defined as “virgin γ -Ga₂O₃” i.e. in the sample fabricated with 1×10^{16} Ni/cm² implants. Accounting that there are practically no deviations in the RBS/C yields for the high fluence implanted samples as compared to that in the virgin γ -Ga₂O₃, we set the relative disorder in the γ -Ga₂O₃ at zero for all high fluences used, see Fig. 1(d) in the main text. Thus, we refer to the RBS/C spectrum obtained upon 1×10^{16} Ni/cm² implants as having the “characteristic shape” to interrelate the rest of the data in Fig. 1.

III. Identification of the newly formed polymorph γ -Ga₂O₃

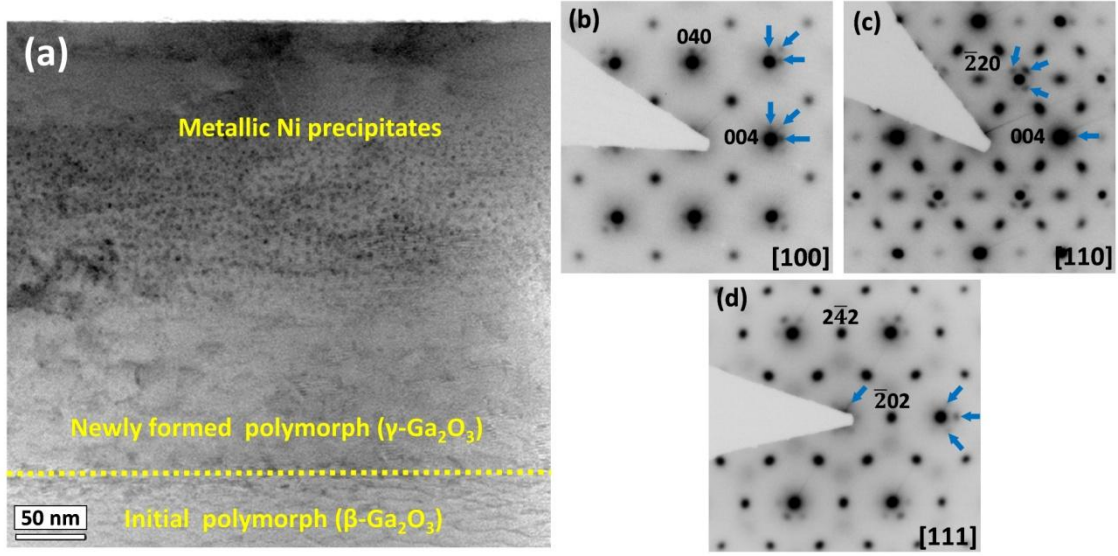


Fig. S3. (a) Low magnification BF-STEM image of the 1×10^{17} Ni/cm² implanted sample together with (b-d) the SAED patterns from the new polymorph layer outside of Ni-precipitation zone. The indexing is according to γ -Ga₂O₃ along the zone axes (b) [100], (c) [110], and (d) [111]. The blue arrows indicate the extra spots described in the text.

Fig. S3(a) show the low magnification BF-STEM images corresponding to the sample implanted with 1×10^{17} Ni/cm². Fig. S3(b-d) show the SAED diagrams indexed according to the γ -Ga₂O₃ polymorph (space group $Fd\bar{3}m$) along the zone axes [100], [110] and [111], respectively. Nevertheless, new findings are observed in the SAED diagrams: the presence of extra weak spots around the family of planes {400}, {440}, {222} and the (000), indicated with a blue arrow, which cannot be indexed according to the cubic γ -Ga₂O₃ polymorph. The cause of these extra spots is due to the presence of cubic metallic Ni (FCC, space group $Fm\bar{3}m$) and a double diffraction effect as a result of the coherence between cubic γ -Ga₂O₃ and cubic Ni metallic precipitates. The diffraction spots related to the metallic Ni are marked in green while the double diffraction spots are indicated with a pink arrow in Fig. 1(c). Similar double diffraction reflections have been reported previously in literature for cubic precipitates inside different matrices [S9,S10].

IV. Formation of metallic Ni precipitates

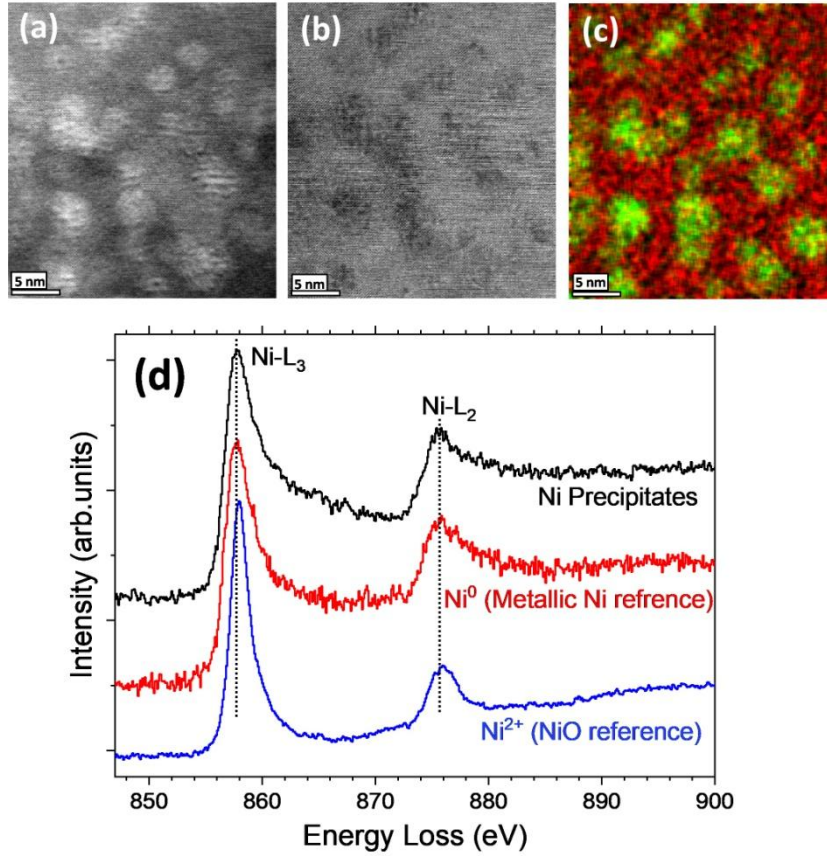


Fig. S4. High Magnification (a) ADF-STEM and (b) BF-STEM of the 1×10^{17} Ni/cm² sample. (c) Corresponding STEM-EDS map acquired for Ga (red) and Ni (green). (d) STEM-EELS Ni L₃ and L₂ edges obtained from the Ni precipitates, metallic Ni reference and NiO reference.

The presence of Ni precipitates inside γ -Ga₂O₃ layer is confirmed by EDS mapping. Fig. S4(a-b) show the ADF and the BF-STEM images at higher magnification revealing the precipitates, respectively. The corresponding EDS map using the Ga-K α line in red together with the Ni-K α in green is shown in Fig. S4(c). In order to know more about the oxidation state, we have recorded an EELS spectrum corresponding to the L_{3,2} line of Ni precipitates, Fig. S4(d), confirming that the precipitates are mainly formed by metallic Ni and not by NiO. A similar line shape has been found before in other articles corresponding to metallic Ni [S11,S12]. Furthermore, for a better comparison, the L_{3,2} Ni line profile of two references corresponding to metallic Ni and NiO are shown as well. The L₃/L₂ ratios obtained were as follows: 1.5, 1.4 and 2.8 for the Ni precipitates, metallic Ni reference and NiO reference, respectively. The good agreement between the stabilized metallic Ni precipitates as a consequence of the implantation and the metallic Ni reference is clear.

V. Low mismatch interface stacking in γ/β -Ga₂O₃ double polymorph structures obtained by ion irradiation

Independently of the type of ions used in the present study we observed the formation of the same stacking at the γ/β -Ga₂O₃ double polymorph structures obtained by ion irradiation. This is illustrated below by applying two different methods for the stacking orientation determinations: STEM and EBSD. For example, in the samples implanted by Au, the orientation relationship between two polymorphs founded in the STEM is γ [100]// β [201], γ [110]// β [132] and γ [112]// β [102]. Fig. S5(a-c) shows schematic representation of γ -Ga₂O₃ (ICSD: 236276 [S13]) and β -Ga₂O₃ (ICSD: 83645 [S14]) along the interphase together with the corresponding diffraction patterns, for the three mentioned orientation relationships.

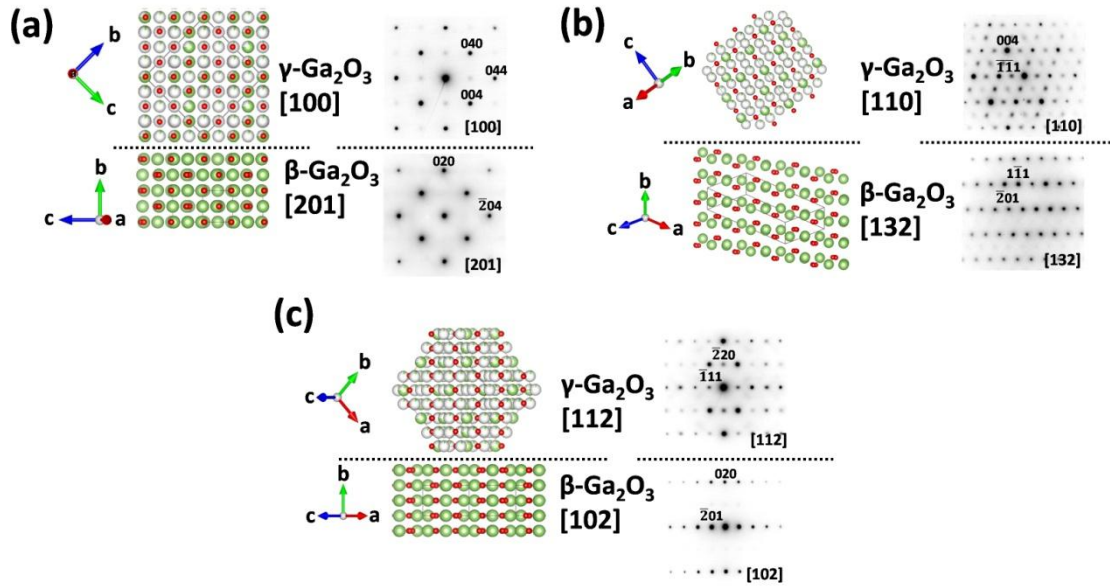


Fig. S5. Schematic representation of: (a) γ -Ga₂O₃ [100]// β -Ga₂O₃ [201], (b) γ [110]// β [132], (c) γ [112]// β [102] along the interphase together with the corresponding diffraction patterns. Color code: Ga (green) O (red). The interphase is represented with a dashed black line.

Interestingly, the lattice mismatch for the stacking in Fig. S5 is quite similar for each zone axis, as summarized in Table SI. This may facilitate the initial β -to- γ transformation as well as the conversion of additional parts of the β -substrate into the γ -film during further accumulation of the dose.

Orientation relationship	Experimental Interplanar distances (Å)
γ [100]// β [201]	γ -Ga ₂ O ₃ $d_{(044)} = 1.47 \pm 0.03$
	β -Ga ₂ O ₃ $d_{(-204)} = 1.46 \pm 0.04$
γ [110]// β [132]	γ -Ga ₂ O ₃ $d_{(-111)} = 4.83 \pm 0.03$
	β -Ga ₂ O ₃ $d_{(-201)} = 4.92 \pm 0.02$
γ [112]// β [102]	γ -Ga ₂ O ₃ $d_{(-1-11)} = 4.78 \pm 0.02$
	β -Ga ₂ O ₃ $d_{(-201)} = 4.82 \pm 0.03$

Table SI. Summary of experimental interplanar distances measured from SAED

For comparison, we also used EBSD on the γ/β -Ga₂O₃ double polymorph structures fabricated with Ne implants. For these measurements, a part of the sample was masked during the irradiation, thus EBSD was performed on both, the unirradiated surface section as well as on the Ne irradiated surface. The mounting of the sample was done so that the β -Ga₂O₃ $\langle 010 \rangle$ lattice direction is aligned parallel to the Z-axis of the SEM reference system, while the β -Ga₂O₃ $\langle 102 \rangle$ lattice direction is aligned parallel to the Y-axis of the SEM reference system. Notably, since both the irradiated and unirradiated parts of the sample underwent exactly the same alignment, the orientation relationship between the unirradiated β -Ga₂O₃ phase and the phase formed after irradiation was only affected by the random error of the EBSD system, which is typically $\leq 1^\circ$ in terms of the misorientation [S16].

Firstly, we found that EBSD patterns recorded in the unirradiated and Ne-irradiated areas of the sample matched with the β -Ga₂O₃ and the γ -Ga₂O₃ polymorph signatures, as illustrated in Figs. S6 (a) and (b), respectively.

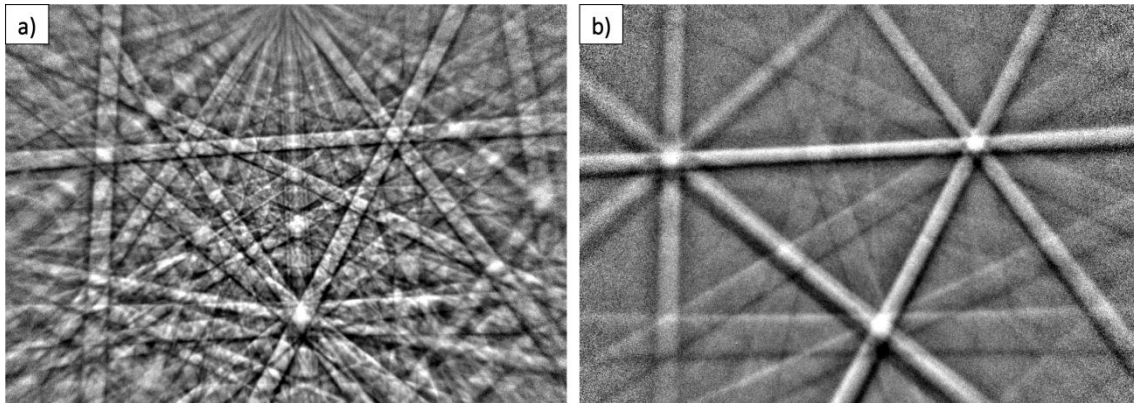


Fig. S6 Recorded EBSD patterns from (a) initial β -Ga₂O₃ and (b) γ -Ga₂O₃ polymorph after Ne irradiation.

The pristine β -Ga₂O₃ crystal gives a high quality EBSD pattern, where many high indexed Kikuchi bands and details inside those are discernible. In comparison, the EBSD pattern quality from the γ -Ga₂O₃ area exhibits less contrast, only low indexed strong intensity bands are clearly distinguishable. A lower EBSD pattern quality may be explained by the intrinsic defective spinel structure of γ -Ga₂O₃ [S17] and not necessarily by addition defects introduced as a consequence of irradiation. However, a quantification from this pattern is not possible. Furthermore, it should be pointed out that EBSD is a surface sensitive method, the depth of the surface layer contributing to the EBSD pattern is of order 10 nm [S18].

Regarding the absolute crystal orientation, the Bruker EBSD software provided the following Euler angles:

β -Ga₂O₃: (309.9°; 89.5°; 358.9°)

γ -Ga₂O₃: (309.9°; 43.6°; 89.0°)

Using these Euler angles an orientation relationship between both phases was calculated to:

β -Ga₂O₃ [100] // γ -Ga₂O₃ [1 -5.6 -1]

β -Ga₂O₃ [010] // γ -Ga₂O₃ [1 0 1]

β -Ga₂O₃ [001] // γ -Ga₂O₃ [-1 0 1]

and

γ -Ga₂O₃ [100] // β -Ga₂O₃ [0 1.9 -1]

γ -Ga₂O₃ [010] // β -Ga₂O₃ [-1.9 -0.1 -1]

γ -Ga₂O₃ [001] // β -Ga₂O₃ [0 2 1]

The fractional numbers indicate that there is an artefact related to the misalignment between low indexed directions of the β -Ga₂O₃ and the γ -Ga₂O₃ polymorphs. This orientation relationship is consistent with results in Fig.S6 obtained by SAED TEM, which indicates that (i) interface stacking in γ/β -Ga₂O₃ double polymorph structures is independent on the ion type used in fabrication process and (ii) it is verified by two different methods.

VI. Defect balance at the β/γ -Ga₂O₃ interface

Fig. 1(a) indicates an increase in thickness of the newly formed γ -Ga₂O₃ layer as a function of the ion fluence. Our interpretation is that there is a disorder threshold for the β -to- γ transition. Thus, the thickness increase of the γ -polymorph in Fig. 1(a) might be a function of the balance between defect generation and annihilation rates at the β/γ -Ga₂O₃ interface. The defect generation rate is a function of the incident beam particles mass, energy and flux. Importantly, all these parameters were kept constant for the data in Fig. 1(a). Otherwise, the amount of the generated defects might obviously scale with the fluence. Therefore, we may try to estimate the DPA threshold required for the polymorph conversion using the SRIM data presented in Fig. S1 and plotting the DPA values at the β/γ interface as a function of the dose. The results of this analysis are shown in Fig. S7. Interestingly, as seen from Fig.S7, the DPA dependence of the β -to- γ transition as measured at the β/γ interface is not constant, as could be expected for a threshold. Instead, it exhibits an increasing trend while the β/γ interface advances deeper into the bulk. It implies that in Fig. S7 we haven't accounted for additional factors governing the defect balance in Fig. 1(a). Indeed, as mentioned above, the residual defect concentration is a balance between the defect generation and annihilation processes. However, as know from literature, the defect annihilation rates are primarily affected by the irradiation temperature [14,S8]. Thus, accounting that the data in Fig. 1(a) were collected at the same temperature, in the first approximation, the assumption of similar annihilation rates in samples implanted with different doses seems to be reasonable (even though we used different beam exposure times which may have affected the diffusion-controlled annihilation). Nevertheless, there should be a reason for the DPA threshold overestimation deeper in the bulk in Fig. S5. Notably, as seen from the inset in Fig. S7, the defect generation rate at the depth of the β/γ interface rapidly decreases with its advance into the bulk of the sample, meaning significant differences for the density of the collision cascades in the samples, even though the “nominal” DPA scales as a function of dose. We believe these cascade density effects – unaccounted in the analysis in Fig.S7 are responsible for the non-constant DPA threshold. This conclusion is also supported by the recent results on the role of the density of collision cascades on the defect formation in β -Ga₂O₃ [S15]. Concurrently, we cannot exclude that the defect balance at the β/γ interface can be affected by the defects diffusion too, altogether, leaving room for further studies paved by our interpretations.

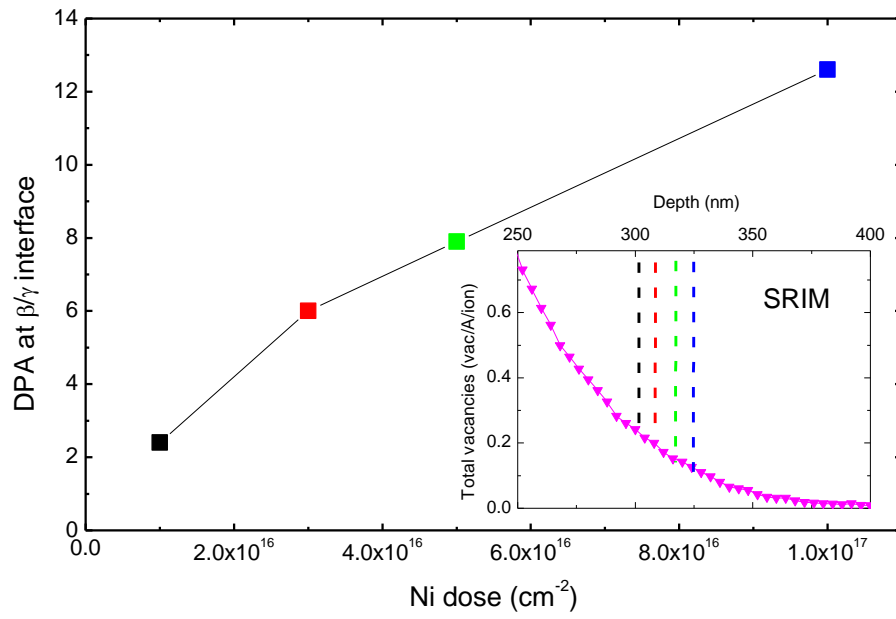


Fig. S7 DPA values calculated at the β/γ interface as a function of the ion dose for the 400 keV Ni irradiations. The inset depicts a part of the SRIM predicted defect generation profile at the depth corresponding to the β/γ interface, using the same color code for the β/γ interface position as that in Fig.1(a).

VII. Impact of Ga sub-lattice non-stoichiometry on the radiation tolerance in γ -Ga₂O₃

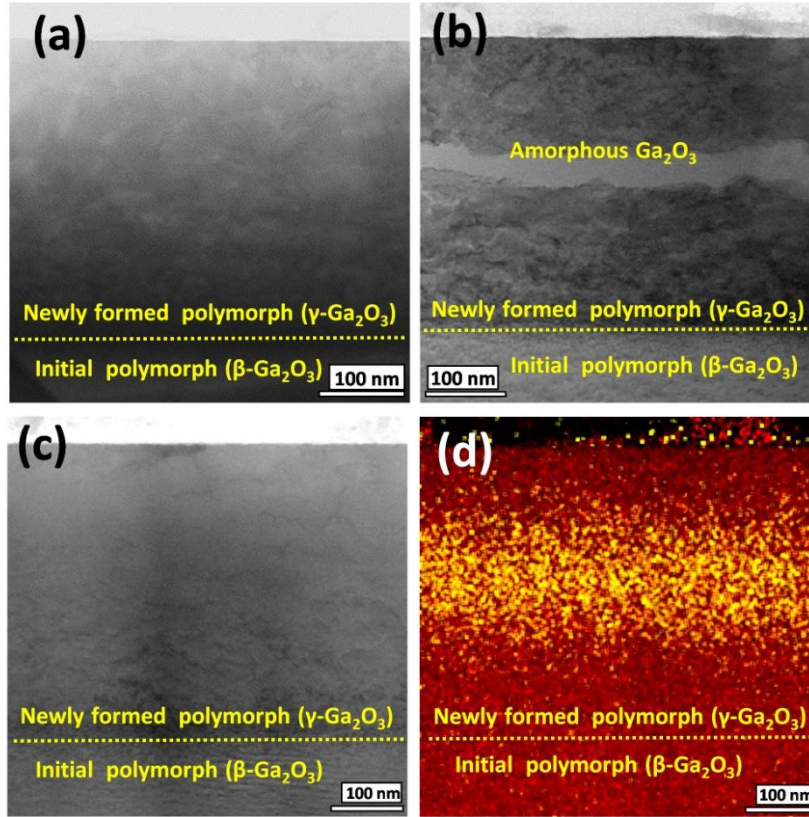


Fig. S8. Low magnification BF-STEM images and EDS maps of Ga and Au implanted γ -Ga₂O₃; (a, b, c) 1×10^{16} Ga/cm², 3×10^{16} Ga/cm² and 1×10^{16} Au/cm² samples, respectively; (d) EDS elemental maps of the 1×10^{16} Au/cm² sample.

Fig. S8 is complimentary to Fig.2 in the main text. As seen from Fig.S8(a) and (b) there is a Ga content threshold for a deviation from the radiation tolerance due to chemical effects. Indeed, three-fold change in the Ga content, corresponding to the dose increase from 1×10^{16} to 3×10^{16} and Ga/cm², implies a dramatic difference in the radiation tolerance behavior, literally the intact crystallinity turns into the amorphization of the middle part of the γ -Ga₂O₃ film, compare Figs. S8(a) and (b). Otherwise, γ -Ga₂O₃ easily tolerates the DPA corresponding to that in Fig.S8(b), if created by other ions, e.g., Au – see Fig. S8(c). We attribute this effect to the increasing deviations from the γ -Ga₂O₃ stoichiometry in Ga sublattice, which is also consistent with the theoretical investigations of the chemical roles of different impurities in Fig.4 of the main text. Meanwhile the elemental distribution of Au is illustrated by the EDS map in Fig. S8(d), using the Ga-K α (red) and Au-L α (yellow) lines.

VIII. Additional details of computational modelling

As shown in Fig. S9(a-b), a detailed comparison of the RDFs and pairwise PRDFs of the pristine β - and γ -Ga₂O₃ lattices reveals that the significant difference lies in the Ga sublattice with the Pearson correlation coefficient, $Pr = 0.762$ (see the Method part of the main text for details). Both the O sublattices of the β - and γ -Ga₂O₃ follow the close-packed face-centered cubic (fcc) stacking, whereas the Ga atoms occupy the tetrahedral and octahedral sites in different symmetries, as shown in Fig. S9(c).

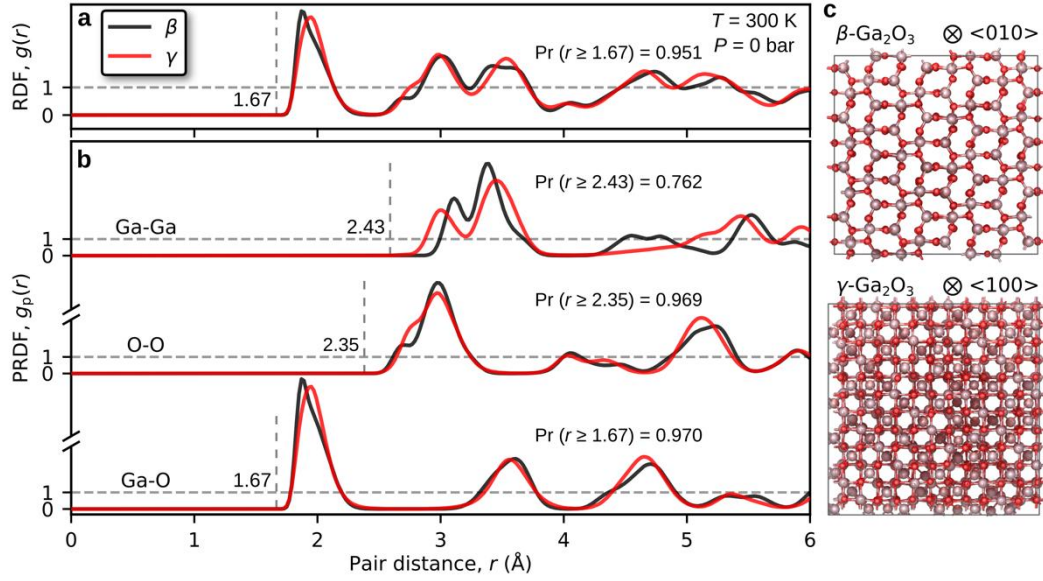


Fig. S9. (a) Total radial distribution functions (RDFs) and (b) pairwise partial RDFs (PRDFs) of the pristine β - and γ -Ga₂O₃ lattices at 300 K and 0 bar. The Pearson correlation coefficients, Pr , between the non-zero parts (ranges from the vertical dashed lines up to 6.0 Å) of the RDF and PRDF curves are shown, revealing that the major difference between the β - and γ -Ga₂O₃ lattices are the configuration of Ga sublattice with rather low Pr of 0.762. (c) Illustration of the pristine β - and γ -Ga₂O₃ supercell with brown Ga and red O atoms

As shown in Fig. S10(a), a further analysis of the 1st and 2nd Ga-Ga shells indicate a high similarity between the two 1st Ga-Ga shells ($\text{Pr} = 0.830$), however, completely uncorrelated 2nd Ga-Ga shells are seen, as the peaks in the β -Ga PRDFs are vanished in the γ -Ga PRDFs ($\text{Pr} = 0.037$). The 1st- and 2nd-shell ordering of the β -Ga sublattice is illustrated in Fig. S10(b-c). In the 1st shell, both the 4-fold (tetrahedral) and 6-fold (octahedral) Ga atoms have 11 Ga neighbors as shown in the zoomed local bonding networks. In the 2nd shell, 4-fold Ga has 8 Ga neighbors, and 6-fold Ga has 6. As a matter of fact, the specific pair between 6-fold Ga and the 6-fold Ga neighbors (shown as the yellow and orange bonds in Fig. S10(c)) contribute to the shallow peak in the β -Ga PRDF around the 4.75 Å (Fig. S10(a)).

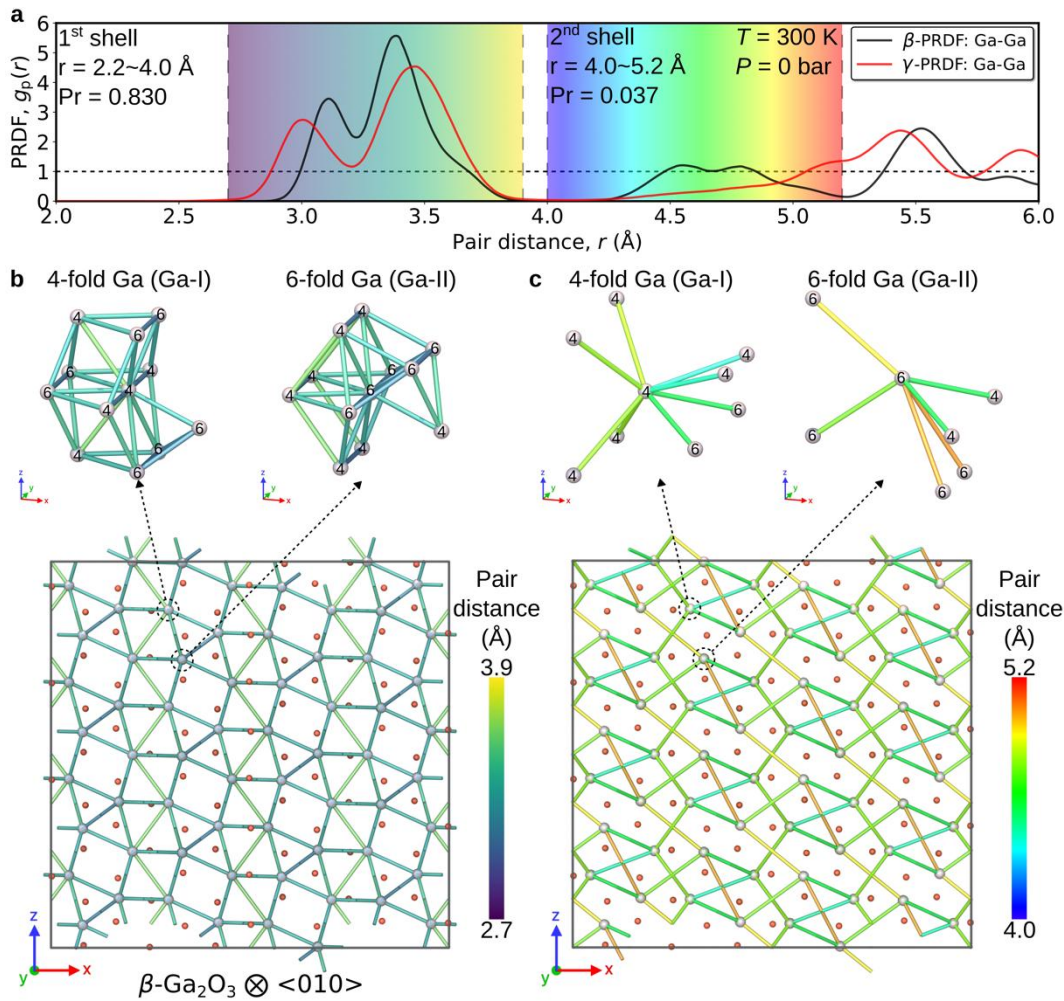


Fig. S10. (a) Ga-Ga PRDFs of the pristine β - and γ -Ga₂O₃ lattices at 300 K and 0 bar with the marked 1st and 2nd Ga-Ga shells of 2.2~4.0 Å and 4.0~5.2 Å, respectively. The range-specified Pr values indicate a high similarity in the 1st Ga-Ga shells of the pristine β - and γ -Ga₂O₃ lattices, whereas a significant difference in the 2nd shells. The two color-coded shadow regions correspond to the two Ga-Ga pair matrices in the β -Ga₂O₃ with visualized bonds, as shown in (b). This 1st-shell short-range ordering of the β -Ga sublattice is randomized in the γ -Ga₂O₃ phase, whereas the 2nd-shell ordering is completely missing.

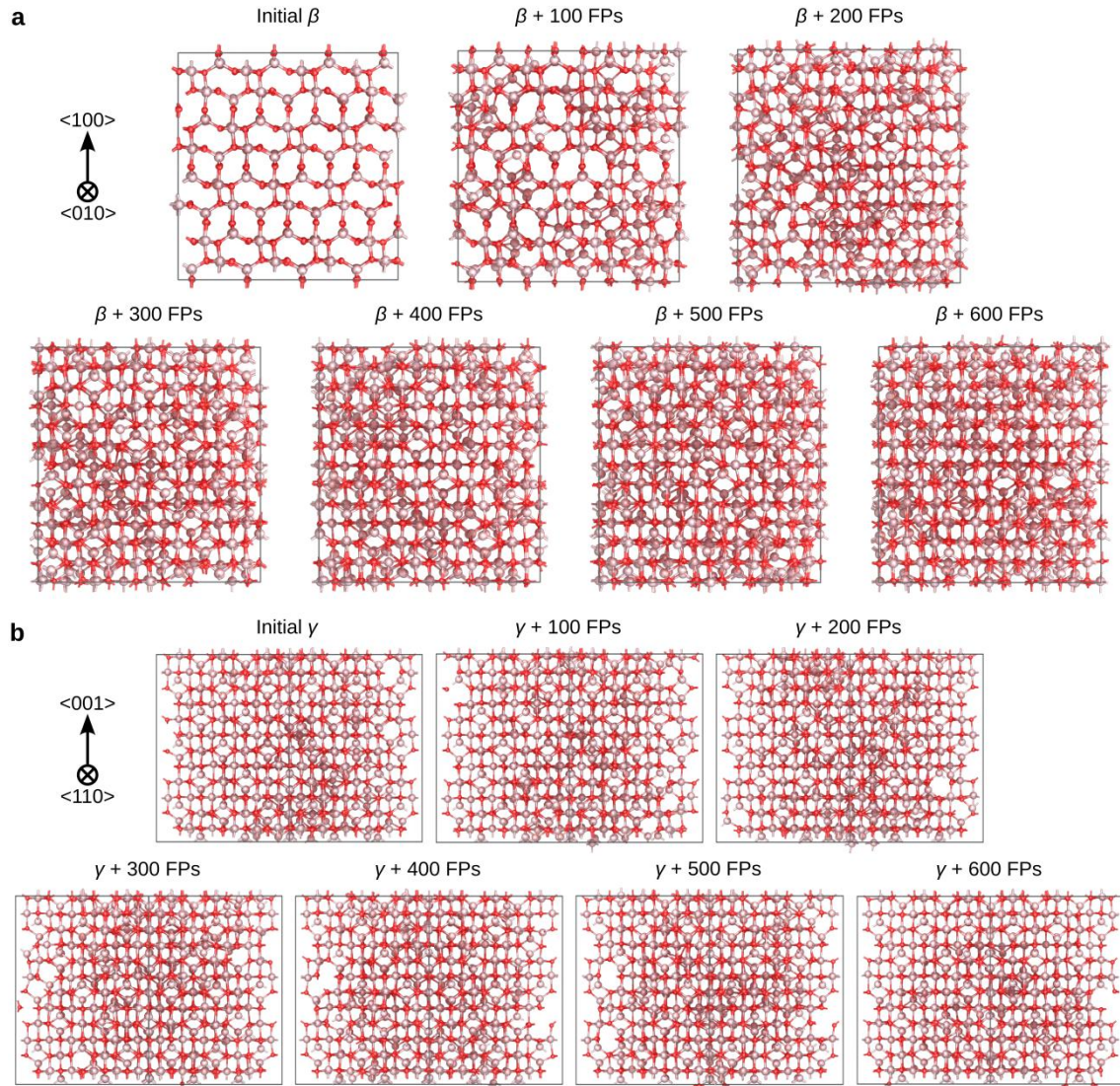


Fig. S11 The snapshots show modifications of the (a) β - Ga_2O_3 and (b) γ - Ga_2O_3 from the pristine lattices up to the lattices with added 600 Frenkel pairs. Ga ions are shown in brown and O in red. Note that the view angle of the γ - Ga_2O_3 here is turned to $\langle 110 \rangle$ (45° turned from $\langle 100 \rangle$ in Fig. 3(b) of the main text), to emphasize the same symmetry of the β/γ -O sublattices.

As shown in Fig. S12, the analysis of the Pearson correlation coefficient reveals the evolution of the structural properties of the Ga sublattices with different numbers of FPs generated. It can be clearly seen that the 1st-shell curves preserve a high similarity ($Pr > 0.800$) for both the β - and γ -Ga₂O₃ owing to the high similarity between initial β/γ curves ($Pr = 0.830$, Fig. S10(a)). On the other hand, the generated FPs have only a marginal effect on the 2nd-shell γ -Ga curves, however, imply dramatic changes onto the 2nd-shell β -Ga curves, indicating a distinct structural transition causing by the cumulated Ga FPs in the β lattice.

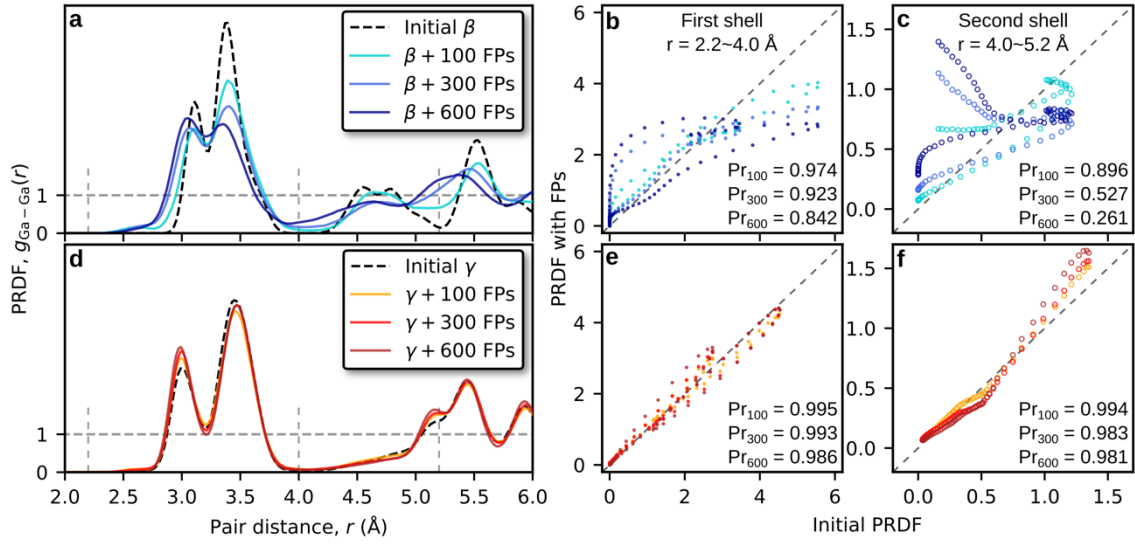


Fig. S12. Detailed Pr analysis: (a, d) The Ga-Ga PRDFs of the β - and γ -Ga₂O₃ lattices after different numbers of FP iterations. The initial β/γ curves are shown as dashed lines for reference. (b-c, e-f) The 1st- and 2nd-shell curves are plotted against the corresponding initial curves. The high similarity of the 1st-shell curves retains after 600 FP iterations, whereas the β -Ga 2nd-shell curves change significantly upon the presenting Ga FPs, and eventually transfer to more γ -like (Fig. 3c-d in the main text).

In Fig. S13, we analyze the stability of the fcc O sublattice during collision cascades. Fig. S12a shows the mean square displacement (MSD) for all Ga and O atoms displaced during the cascades. By increasing the threshold displacement (the minimal displacement distance that is counted in the calculation of MSD) we reveal stronger mobility of O ions during the cascades. The red curve that plots the MSD values for O atoms is much higher than the black curve, indicating that O atoms were displaced in cascades much more efficiently. This is also seen in the exemplary snapshots at different time instances of the cascade evolution (0, 0.2, 2.5 and 50 ps) that reveal formation of large amount of coordination defects during the cascade, which practically fully disappear in the O sublattice leaving behind only very few vacancy clusters. Given long time between the ion impacts in standard ion accelerators, these remaining defects are expected to recover further given the strength of the O sublattice, which we observe in our simulations.

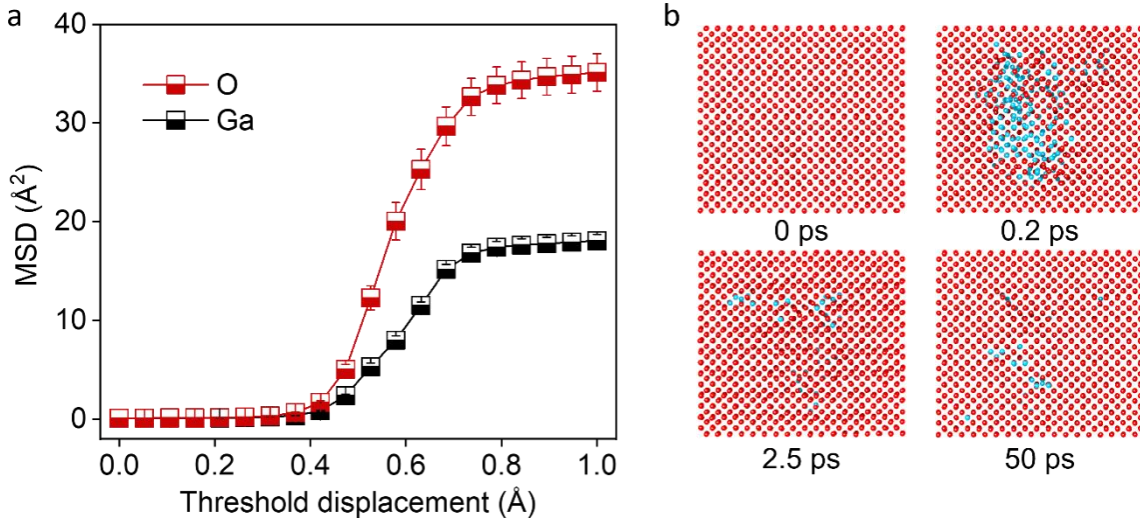


Fig. S13 (a) Mobility of the Ga and O ions during the collision cascades plotted as the mean square displacement (MSD) found from the comparison of the atoms in the first and the last (50 ps) frame after the cascade. The MSD is plotted as a function of the threshold displacement, therefore, only atoms with the final displacement larger than the threshold value are included in the statistics. The error bars are the standard error of the mean collected in 120 MD simulations. (b) The snapshots showing the evolution of the fcc O sublattice at different time instances during an exemplary cascade case. The oxygen ions are colored according to the coordination number (the red color is used for the ions with $Z = 11$ (with one neighboring vacancy) or 12 (perfect fcc), to exclude coloring of atoms around single vacancies, which do not distort the lattice).

In Figs. S14 and S15, the AIMD runs were conducted with an initial 160-atom γ -Ga₂O₃ cell with additional 8/12/16 inserted Ni/Au/Ga atoms, which corresponds to 5/7.5/10 at.% of foreign ion excess, respectively. The quantitative analyses shown in Figs. S14(d)-(e), and S15(d) were done in the same way than of that in Fig. 4 of the main text.

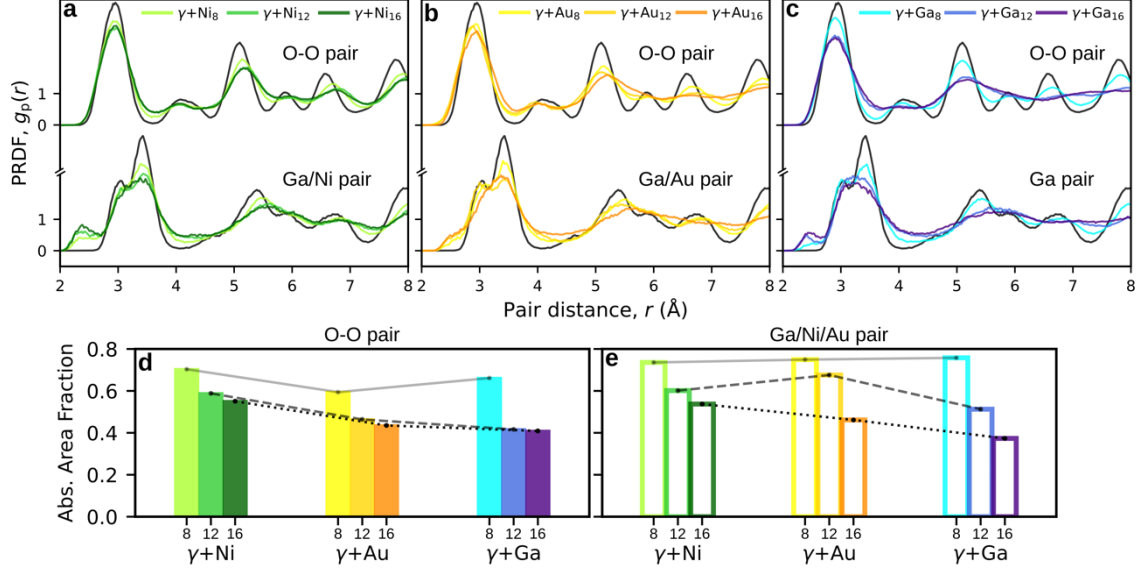


Fig. S14 (a-c) AIMD-PRDFs of O-O and heavy-ion (Ga/Ni/Au) pairs at 900 K and 0 bar, with different concentrations of the foreign ions. The first valleys are at 3.6 and 4.0 Å, as the same as those labelled in Fig. 4a of the main text. (d, e) Ratios of the absolute areas (covered by the PRDF curves with reference to 1): the distorted cells against the initial γ cell.

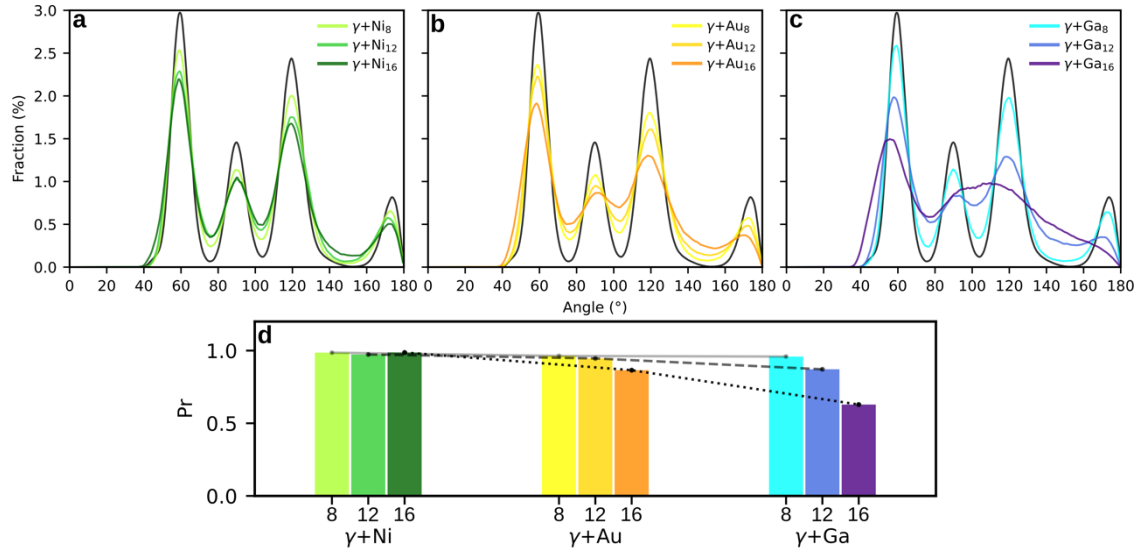


Fig. S15 (a-c) Bond angle distribution of O sublattice with O-O bond cutoff at 3.6 Å, with different concentrations of the foreign ions. The black curves are the pristine ones without the foreign ions. (d) The Pr values of the distorted bond-angle distribution to the one of the initial γ cell.

References:

- S1. A. I. Titov, A. Yu. Azarov, L. M. Nikulina, and S. O. Kucheyev, “Damage buildup and the molecular effect in Si bombarded with PF_n cluster ions”, Nucl. Instrum. Methods Phys. Res. B **256**, 207 (2007).
- S2. J. F. Ziegler, M. D. Ziegler, and J. P. Biersack, “SRIM—the stopping and range of ions in matter (2010)”, Nucl. Instrum. Methods Phys. Res. B **268**, 1818 (2010).
- S3. γ -Ga₂O₃ Crystal Structure. Inorganic Solid Phases, SpringerMaterials (online database), Heidelberg (ed.) (https://materials.springer.com/isp/crystallographic/docs/sd_1201199).
- S4. A. Azarov, C. Baziotti, V. Venkatachalapathy, P. Vajeeston, E. Monakhov, and A. Kuznetsov, “Disorder-induced ordering in gallium oxide polymorphs”, Phys. Rev. Lett. **128**, 015704 (2022).
- S5. E. A. Anber, D. Foley, A. C. Lang, J. Nathaniel, J. L. Hart, M. J. Tadjer, K. D. Hobart, S. Pearton, and M. L. Taheri, “Structural transition and recovery of Ge implanted β -Ga₂O₃”, Appl. Phys. Lett. **117**, 152101 (2020).
- S6. J. García-Fernández, S. B. Kjeldby, P. D. Nguyen, O. B. Karlsen, L. Vines, and III. Prytz, ” Formation of γ -Ga₂O₃ by ion implantation: Polymorphic phase transformation of β -Ga₂O₃” Appl. Phys. Lett. **121**, 191601 (2022).
- S7. T. Yoo, X. Xia, F. Ren, A. Jacobs, M. J. Tadjer, S. Pearton, and H. Kim, “Atomic-scale characterization of structural damage and recovery in Sn ion-implanted β -Ga₂O₃”, Appl. Phys. Lett. **121**, 072111 (2022).
- S8. A. Azarov, V. Venkatachalapathy, I.-H. Lee, and A. Kuznetsov, “Thermal versus radiation-assisted defect annealing in β -Ga₂O₃”, J. Vac. Sci. Technol. A **41**, 023101 (2023).
- S9. M. Hecz, D. Esser, T. M. Smith, P. Beran, V. Mazánová, D. W. McComb, T. Kruml, J. Polák, and M. J. Mills, “Atomic resolution characterization of strengthening nanoparticles in a new high-temperature-capable 43Fe-25Ni-22.5Cr austenitic stainless steel”, Mater. Sci. Eng. A **719**, 49 (2018).
- S10. Y. Wang and W. Zhang, “Mapping the strain distribution within embedded nanoparticles via geometrical phase analysis”, Micron **125**, 102715 (2019).
- S11. Ø. Prytz, J. Taftø, C.C. Ahn, and B. Fultz, “Transition metal d-band occupancy in skutterudites studied by electron energy-loss spectroscopy”, Phys. Rev. B **75**, 125109 (2007).
- S12. G. Radtke, M. Hennes, M. Bugnet, Q. M. Ramasse, X. Weng, D. Demaille, B. Gobaut, P. Ohresser, E. Otero, F. Choueikani, A. Juhin, P. Saintavit, Y. Zheng, and F. Vidal, “Atomic-scale study of metal–oxide interfaces and magnetoelastic coupling in self-assembled epitaxial vertically aligned magnetic nanocomposites”, Adv. Mater. Interfaces **6**, 1900549 (2019).
- S13. H. Y. Playford, A. C. Hannon, E. R. Barney, and R. I. Walton, “Structures of Uncharacterised Polymorphs of Gallium Oxide from Total Neutron Diffraction”, Chem. - Eur. J. **19**, 2803 (2013).
- S14. J. Ahman, G. Svensson, and J. Albertsson, “A reinvestigation of β -gallium oxide”, Acta Crystallogr., Sect. C: Cryst. Struct. Commun. **52**, 1336 (1996).
- S15. A. Azarov, V. Venkatachalapathy, P. Karaseov, A. Titov, K. Karabeshkin, A. Struchkov, and A. Kuznetsov, “Interplay of the disorder and strain in gallium oxide”, Sci. Rep. **12**, 15366 (2022).
- S16. P. Chekhonin, J. Engelmann, C.-G. Oertel, B. Holzapfel, and W. Skrotzki, “Relative angular precision in electron backscatter diffraction: A comparison between cross correlation and Hough transform based analysis”, Cryst. Res. Technol. **49**, 435 (2014).
- S17. L. E. Ratcliff, T. Oshima, F. Nippert, B. M. Janzen, E. Kluth, R. Goldhahn, M. Feneberg, P. Mazzolini, O. Bierwagen, C. Wouters, M. Nofal, M. Albrecht, J. E. N. Swallow, L. A. H. Jones, P. K. Thakur, T.-L. Lee, C. Kalha, C. Schlueter, T. D. Veal, J. B. Varley, M. R. Wagner, and A. Regoutz, “Tackling Disorder in γ -Ga₂O₃”, Adv. Mater. **34**, 2204217 (2022).
- S18. S. Zaefferer, “On the formation mechanisms, spatial resolution and intensity of backscatter Kikuchi patterns”, Ultramicroscopy **107**, 254 (2007).
- S19. K. Schmid, “Some new aspects for the evaluation of disorder profiles in silicon by backscattering”, Radiat. Eff. **17**, 201 (1973).